New Central and Central Discontinuous Galerkin Schemes on Overlapping Cells of Unstructured Grids for Solving Ideal Magnetohydrodynamic Equations with Globally Divergence-Free Magnetic Field

Zhiliang Xu [‡] and Yingjie Liu [§]

September 12, 2016

Abstract

New schemes are developed on triangular grids for solving ideal magnetohydrodynamic equations while preserving globally divergence-free magnetic field. These schemes incorporate the constrained transport (CT) scheme of Evans and Hawley [39] with central schemes and central discontinuous Galerkin methods on overlapping cells which have no need for solving Riemann problems across cell edges where there are discontinuities of the numerical solution. These schemes are formally second-order accurate with major development on the reconstruction of globally divergence-free magnetic field on polygonal dual mesh. Moreover, the computational cost is reduced by solving the complete set of governing equations on the primal grid while only solving the magnetic induction equation on the polygonal dual mesh. Various numerical experiments are provided to validate the new schemes.

1 Introduction

The ideal magnetohydrodynamic (MHD) equations describe the dynamics of electrically conducting fluids and have wide applications in fields like astrophysics and laboratory plasmas. In two-dimensional (2D) space, the ideal MHD equations written in the conservative form are

[‡](E-mail: zxu2@nd.edu)
Department of Applied and Computational Mathematics and Statistics, University of Notre Dame, Notre Dame, IN 46556. Research was supported in part by NSF grant DMS-1517293.

[§](E-mail: yingjie@math.gatech.edu)
School of Mathematics, Georgia Institute of Technology, Atlanta, GA 30332. Research supported in part by NSF grant DMS-1522585.

$$\partial_t \begin{pmatrix} \rho \\ \rho u_x \\ \rho u_y \\ \rho u_z \\ \varepsilon \\ B_x \\ B_y \\ B_z \end{pmatrix} + \partial_x \begin{pmatrix} \rho u_x \\ \rho u_x^2 + p - B_x^2 \\ \rho u_x u_y - B_x B_y \\ \rho u_x u_z - B_x B_z \\ (\varepsilon + p) u_x - B_x (\mathbf{u} \cdot \mathbf{B}) \\ 0 \\ (u_x B_y - u_y B_x) \\ -(u_z B_x - u_x B_z) \end{pmatrix} + \partial_y \begin{pmatrix} \rho u_y \\ \rho u_x u_y - B_x B_y \\ \rho u_y^2 + p - B_y^2 \\ \rho u_y u_z - B_y B_z \\ (\varepsilon + p) u_y - B_y (\mathbf{u} \cdot \mathbf{B}) \\ -(u_x B_y - u_y B_x) \\ 0 \\ (u_y B_z - u_z B_y) \end{pmatrix} = \mathbf{0} \ . \quad (1.1)$$

Here ρ is the fluid density, $\mathbf{u} = (u_x, u_y, u_z)^t$ is the velocity, $\mathbf{B} = (B_x, B_y, B_z)^t$ is the magnetic field, ε is the total energy density, $p = p_{gas} + \mathbf{B} \cdot \mathbf{B}/2$ is the total pressure and p_{gas} is the hydrodynamic gas pressure. In this paper, p_{gas} is assumed to satisfy the following equation of state

$$p_{gas} = (\gamma - 1)(\varepsilon - \frac{1}{2}\rho \mathbf{u} \cdot \mathbf{u} - \frac{1}{2}\mathbf{B} \cdot \mathbf{B}) \ ,$$

where γ is the adiabatic index. The electric field $\mathbf{E}$ is given by $\mathbf{E} = -\mathbf{u} \times \mathbf{B}$. We also use the notation $\mathbf{x} \equiv (x, y)$ for spatial variables in 2D.

The magnetic field $\mathbf{B}$ is supposed to be divergence-free at any time

$$\nabla \cdot \mathbf{B} = 0 \ . \quad (1.2)$$

However the divergence-free constraint (1.2) introduces additional difficulty in solving Eq. (1.1) numerically. If $\nabla \cdot \mathbf{B}$ is not exactly zero and increases with time, unphysical solutions in which magnetic field lines have wrong topologies leading to plasma transport orthogonal to the magnetic field could occur. See also references [3, 7, 34, 25] for related discussions.

To design schemes for solving the ideal MHD equations, many efforts have been devoted to developing techniques to ensure the divergence-free evolution of the magnetic field. To name a few, these include Hodge projection approach [3], Powell's source term formulation [6], constrained transport (CT) methods [39, 23, 24], locally divergence-free discontinuous Galerkin (DG) [12, 13], central scheme [10, 11] and central DG on overlapping cells of Cartesian grid [14, 15], and many others [25, 28, 42, 44, 43, 45, 46, 48]. We apologize in advance to the many important contributors whose work could not be explicitly mentioned in this paper.

The central scheme on overlapping cells [16] eliminates excessive numerical dissipation for small time steps of the central scheme of Nessyahu and Tadmor [27] by taking staggered meshes as a collection of overlapping cells and computing solutions by overlapping cell averages. This scheme is used along with the CT method by Li [10, 11] to solve the MHD equations without having to deal with Riemann problems, in particular for the electric field because of the use of overlapping cells. In [17] the central DG scheme on overlapping cells has been developed, extending the work [16] to finite element methods. General schemes with arbitrary orders of accuracy, which combine ideas of the CT approach and central DG schemes on overlapping cells to solve ideal MHD equations, have been developed for rectangular grids in [14, 15] in which the numerical magnetic field is evolved in an exactly divergence-free manner.

In this paper, we develop second-order accurate central and central DG schemes for solving ideal MHD equations on triangular grids. The essential ingredients of these two schemes consist of ideas of central schemes or central DG finite element schemes on overlapping cells, a non-staggered central scheme [9], the TVD Runge-Kutta (RK) time discretization [29, 8], and new exactly divergence-free reconstruction of the numerical magnetic field on both grids.

Several new ideas are introduced in this paper: 1) A new non-staggered central scheme combining strategies of [9] and [16] is presented. This scheme removes $O\left(\frac{1}{\Delta t^n}\right)$ dependency of numerical dissipation associated with the non-staggered central scheme [9]. 2) Although a triangular grid (or primal grid) and its dual grid are utilized complying the basic ideas of the central schemes on overlapping cells [16, 17], on the dual grid only the magnetic induction equation of system (1.1) is defined on the grid edges using the CT formulation; while the full set of governing equations (1.1) is only solved on the triangular grid. This setup reduces the computational cost by almost one half compared with the central or central DG schemes on overlapping cells [10, 11, 14, 15] for solving the ideal MHD equations in which the full set of governing equations (1.1) is solved on both grids. 3) The globally divergence-free magnetic field supported on the dual grid on the next time level is computed using the CT approach and reconstructed by using a new reconstruction procedure. Another new reconstruction procedure developed in the paper and the new non-staggered central scheme combining ideas of [9] and [16] are used to reconstruct the globally divergence-free magnetic field supported on the triangular mesh from the one defined on the dual grid. 4) Using our method, there is no need to solve the multi-dimensional Riemann problem [42, 44, 43, 45, 46] for computing the electric field defined on grid nodes when using the CT formulation.

The rest of the paper is organized as follows: Section 2 describes the new non-staggered central scheme approach combining [9] and [16] for solving conservation laws. Section 3 describes implementation of the new central DG scheme for solving the ideal MHD equations. Section 4 is devoted to presenting the new central scheme for solving the ideal MHD equations. Section 5 outlines the limiting algorithm. Numerical tests are presented in Section 6. Finally, conclusions are discussed in Section 7.

2 New Non-Staggered Central Scheme Formation

2.1 Review of central schemes

We first review the basic ideas of the non-staggered central scheme [9] and the central scheme on overlapping cells [16]. Consider a one-dimensional scalar conservation law $\partial_t u + \partial_x f(u) = 0$ and a grid $\cdots < x_i < x_{i+1} < x_{i+2} < \cdots$. Let $x_{i+1/2} = \frac{1}{2}(x_i + x_{i+1})$, and denote cells $\mathcal{K}_{i+1/2} = (x_i, x_{i+1})$ and $\mathcal{D}_i = (x_{i-1/2}, x_{i+1/2})$ for any i.

A forward Euler step of the non-staggered central scheme [9] can be described as follows. Suppose at the time t^n, the approximate cell average of u on cell $\mathcal{K}_{i+1/2}$ is given as $\overline{U}^n_{i+1/2}$ for any i. A reconstruction procedure can be applied to obtain a piecewise polynomial function $\tilde{U}(x)$ approximating $u(x, t^n)$. $\tilde{U}(x)$ restricted on cell $\mathcal{K}_{i+1/2}$ is a polynomial for any i. The

cell average $\overline{V}_i^{n+1}$ on cell $\mathcal{D}_i$ at the time t^{n+1} is computed as

$$\overline{V}_i^{n+1} = \frac{1}{x_{i+1/2} - x_{i-1/2}} \int_{x_{i-1/2}}^{x_{i+1/2}} \tilde{U}(x)dx - \frac{\Delta t^n}{x_{i+1/2} - x_{i-1/2}} \left[f(\tilde{U}(x_{i+1/2})) - f(\tilde{U}(x_{i-1/2})) \right] , \ \forall i , \tag{2.1}$$

where $\Delta t^n = t^{n+1} - t^n$. Another reconstruction procedure can be applied to the cell averages $\{\overline{V}_i^{n+1}\}$ to obtain a piecewise polynomial function $\tilde{V}(x)$, of which the restriction on cell $\mathcal{D}_i$ is a polynomial for any i. Finally the new cell average $\overline{U}_{i+1/2}^{n+1}$ on cell $\mathcal{K}_{i+1/2}$ at the time t^{n+1} is obtained by averaging $\tilde{V}(x)$ over cell $\mathcal{K}_{i+1/2}$, for any i.

The central scheme on overlapping cells [16] begins with the approximate cell averages of $u(x,t)$ at the time t^n, $\overline{U}_{i+1/2}^n$ and $\overline{V}_i^n$, on cell $\mathcal{K}_{i+1/2}$ and $\mathcal{D}_i$, respectively, for any i. A reconstruction procedure can be applied to these cell averages to obtain a piecewise polynomial function $\tilde{U}(x)$ approximating $u(x,t^n)$, which restricted on cell $\mathcal{K}_{i+1/2}$ is a polynomial for any i; and another piecewise polynomial function $\tilde{V}(x)$ approximating $u(x,t^n)$, which restricted on cell $\mathcal{D}_i$ is a polynomial for any i. Note that we are describing a different scheme in this paragraph, though we still use notations similar to those in the above description of the non-staggered central scheme [9] for convenience. The new cell averages at the time t^{n+1} on overlapping cells can be computed as

$$\begin{aligned} \overline{V}_i^{n+1} &= \frac{\theta}{x_{i+1/2} - x_{i-1/2}} \int_{x_{i-1/2}}^{x_{i+1/2}} \tilde{U}(x)dx + \\ &\quad (1-\theta)\overline{V}_i^n - \frac{\Delta t^n}{x_{i+1/2} - x_{i-1/2}} \left[f(\tilde{U}(x_{i+1/2})) - f(\tilde{U}(x_{i-1/2})) \right] , \quad \forall i , \end{aligned}$$

and

$$\begin{aligned} \overline{U}_{i+1/2}^{n+1} &= \frac{\theta}{x_{i+1} - x_i} \int_{x_i}^{x_{i+1}} \tilde{V}(x)dx + \\ &\quad (1-\theta)\overline{U}_{i+1/2}^n - \frac{\Delta t^n}{x_{i+1} - x_i} \left[f(\tilde{V}(x_{i+1})) - f(\tilde{V}(x_i)) \right] , \quad \forall i , \end{aligned}$$

where $\theta = (t^{n+1} - t^n)/\Delta\tau^n$, $\Delta\tau^n$ is the largest possible time step size determined by the CFL condition. The semi-discrete form can be easily obtained as follows (to which a Runge-Kutta or other time discretization methods can be applied)

$$\begin{aligned} \frac{d}{dt}\overline{V}_i \Big|_{t=t^n} &= \frac{1}{\Delta\tau^n} \left[\frac{1}{x_{i+1/2} - x_{i-1/2}} \int_{x_{i-1/2}}^{x_{i+1/2}} \tilde{U}(x)dx - \overline{V}_i^n \right] - \\ &\quad \frac{1}{x_{i+1/2} - x_{i-1/2}} \left[f(\tilde{U}(x_{i+1/2})) - f(\tilde{U}(x_{i-1/2})) \right] , \quad \forall i , \end{aligned}$$

and

$$\begin{aligned} \frac{d}{dt}\overline{U}_{i+1/2} \Big|_{t=t^n} &= \frac{1}{\Delta\tau^n} \left[\frac{1}{x_{i+1} - x_i} \int_{x_i}^{x_{i+1}} \tilde{V}(x)dx - \overline{U}_{i+1/2}^n \right] - \\ &\quad \frac{1}{x_{i+1} - x_i} \left[f(\tilde{V}(x_{i+1})) - f(\tilde{V}(x_i)) \right] , \quad \forall i . \end{aligned}$$

The semi-discrete form demonstrates that there is no $O\left(\frac{1}{\Delta t^n}\right)$ error commonly associated with the staggered averaging. In the following new scheme, this idea is applied to the previous non-staggered central scheme [9] to remove its $O\left(\frac{1}{\Delta t^n}\right)$ error.

2.2 New non-staggered central scheme

Suppose at the time t^n, the approximate cell average of $u(x,t^n)$ on cell $\mathcal{K}_{i+1/2}$ is given as $\overline{U}^n_{i+1/2}$ for any i, and the approximate cell average of $u(x,t^n)$ on cell $\mathcal{D}_i$ is given as $\overline{V}^n_i$ for any i. A reconstruction procedure can be applied to obtain a piecewise polynomial function $\tilde{U}(x)$ approximating $u(x,t^n)$. $\tilde{U}(x)$ restricted on cell $\mathcal{K}_{i+1/2}$ is a polynomial for any i. The cell average $\overline{V}^{n+1}_i$ on cell $\mathcal{D}_i$ at the time t^{n+1} is computed as

$$\begin{aligned} \overline{V}^{n+1}_i &= \frac{\theta}{x_{i+1/2}-x_{i-1/2}}\int_{x_{i-1/2}}^{x_{i+1/2}} \tilde{U}(x)dx + \\ &\quad (1-\theta)\overline{V}^n_i - \frac{\Delta t^n}{x_{i+1/2}-x_{i-1/2}}\left[f(\tilde{U}(x_{i+1/2})) - f(\tilde{U}(x_{i-1/2}))\right] \ , \quad \forall i \ , \end{aligned} \tag{2.2}$$

where $\theta = (t^{n+1}-t^n)/\Delta\tau^n \in [0,1]$, $\Delta\tau^n$ is the largest possible time step size determined by the CFL condition. The semi-discrete form is described as follows

$$\begin{aligned} \frac{d}{dt}\overline{V}_i\Big|_{t=t^n} &= \frac{1}{\Delta\tau^n}\left[\frac{1}{x_{i+1/2}-x_{i-1/2}}\int_{x_{i-1/2}}^{x_{i+1/2}}\tilde{U}(x)dx - \overline{V}^n_i\right] - \\ &\quad \frac{1}{x_{i+1/2}-x_{i-1/2}}\left[f(\tilde{U}(x_{i+1/2})) - f(\tilde{U}(x_{i-1/2}))\right] \ , \quad \forall i \ . \end{aligned}$$

After obtaining the cell average $\overline{V}^{n+1}_i$ for every i, another reconstruction procedure can be applied to these averages to obtain a piecewise polynomial function $\tilde{V}(x)$, which restricted on cell $\mathcal{D}_i$ is a polynomial for any i. Finally the new cell average $\overline{U}^{n+1}_{i+1/2}$ on cell $\mathcal{K}_{i+1/2}$ at the time t^{n+1} is obtained by averaging $\tilde{V}(x)$ over cell $\mathcal{K}_{i+1/2}$, for any i. Note that the forward Euler component step (2.2) can be reformulated as a convex combination of the non-staggered central scheme [9] and the solution at the previous time V^n_i

$$\begin{aligned} &\overline{V}^{n+1}_i = (1-\theta)\overline{V}^n_i + \\ &\quad \theta\left\{\frac{1}{x_{i+1/2}-x_{i-1/2}}\int_{x_{i-1/2}}^{x_{i+1/2}}\tilde{U}(x)dx - \frac{\Delta\tau^n}{x_{i+1/2}-x_{i-1/2}}\left[f(\tilde{U}(x_{i+1/2})) - f(\tilde{U}(x_{i-1/2}))\right]\right\} \ , \ \forall i \ . \end{aligned} \tag{2.3}$$

Therefore we have the following theorem.

Theorem. If the forward Euler step (2.1) of the non-staggered central scheme [9] is TVD (with a suitable nonlinear reconstruction procedure) with the time step size $\Delta\tau^n$, then the new scheme (2.2) is also TVD for any time step size Δt^n satisfying $0 \le \Delta t^n \le \Delta\tau^n$.

3 Central DG Scheme Formulation for Solving Ideal MHD Equations

In this section, we present the new central DG scheme on overlapping cells for solving the ideal MHD equations. For simplicity, we use the forward Euler method as the time discretization method during the discussion. Higher-order accuracy in time can be achieved by using the TVD RK method [29, 8] or the strong stability preserving method [26].

The physical domain $\Omega \subset R^2$ is partitioned into a collection of triangular cells

$$\mathcal{T}_h = \{\mathcal{K}_i, i = 1, ..., \mathcal{N}_\mathcal{T}\} \tag{3.1}$$

so that $\Omega = \bigcup_{i=1}^{\mathcal{N}_\mathcal{T}} \mathcal{K}_i$. $\mathcal{T}_h$ is the primal mesh. For simplicity, we assume that no vertex of one triangle lies on the interior of an edge of another triangle.

Let the dual grid of $\mathcal{T}_h$ be $\mathcal{W}_h = \{\mathcal{D}_j, j = 1, ..., \mathcal{N}_\mathcal{W}\}$. $\mathcal{D}_j$ is formed by joining centroids of triangles meeting at a common grid node of $\mathcal{T}_h$. Each dual grid cell is further partitioned into a set of **partial cells**. See Fig. 1 for example. Dual cell $\mathcal{D}_1$ is partitioned into a collection of partial cells denoted as $T_{1,1}, T_{2,1}, \ldots, T_{6,1}$ formed by connecting individual vertices $V1, V2, \ldots, V6$ of $\mathcal{D}_1$ with the node O of grid $\mathcal{T}_h$, respectively. Vertices $V1, V2, \ldots, V6$ are centroids of triangular cells $\mathcal{K}_1, \mathcal{K}_2, \ldots, \mathcal{K}_6$ of the primal mesh. These partial cells will be used when the globally divergence-free magnetic field on $\mathcal{W}_h$ is reconstructed.

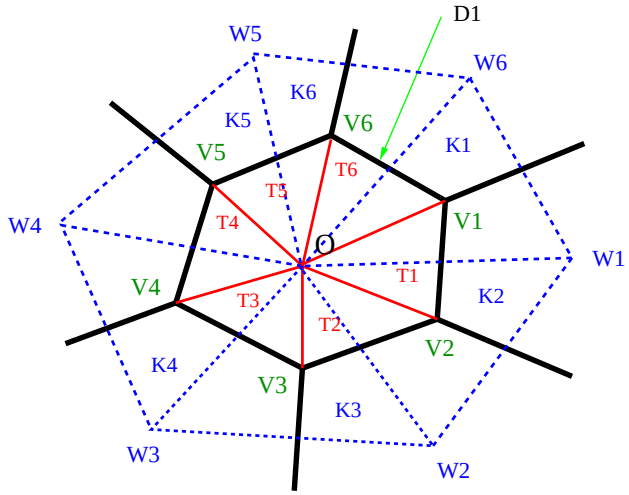

Figure 1: Schematic of overlapping grid.

For the convenience of discussion, we introduce two vectors $\mathbf{U} = (\rho, \rho u_x, \rho u_y, \rho u_z, \varepsilon, B_z)^t$ and $\mathbf{B}^B = (B_x, B_y)^t$, and rewrite Eq. (1.1) as a combination of two sub-systems, namely, Eq. (3.2) and Eq. (3.4), respectively.

Here

$$\partial_t \mathbf{U} + \partial_x \mathbf{F}(\mathbf{U}, \mathbf{B}^B) + \partial_y \mathbf{G}(\mathbf{U}, \mathbf{B}^B) = \mathbf{0} \ , \tag{3.2}$$

where

$$\mathbf{F}(\mathbf{U}, \mathbf{B}^B) = \begin{pmatrix} \rho u_x \\ \rho u_x^2 + p - B_x^2 \\ \rho u_x u_y - B_x B_y \\ \rho u_x u_z - B_x B_z \\ (\varepsilon + p) u_x - B_x (\mathbf{u} \cdot \mathbf{B}) \\ -(u_z B_x - u_x B_z) \end{pmatrix} \ , \quad \mathbf{G}(\mathbf{U}, \mathbf{B}^B) = \begin{pmatrix} \rho u_y \\ \rho u_x u_y - B_x B_y \\ \rho u_y^2 + p - B_y^2 \\ \rho u_y u_z - B_y B_z \\ (\varepsilon + p) u_y - B_y (\mathbf{u} \cdot \mathbf{B}) \\ (u_y B_z - u_z B_y) \end{pmatrix} . \tag{3.3}$$

And

$$\partial_t \mathbf{B}^B + \partial_x \mathbf{F}^B(\mathbf{U}, \mathbf{B}^B) + \partial_y \mathbf{G}^B(\mathbf{U}, \mathbf{B}^B) = \mathbf{0} \ , \tag{3.4}$$

where

$$\mathbf{F}^B(\mathbf{U}, \mathbf{B}^B) = \begin{pmatrix} 0 \\ u_x B_y - u_y B_x \end{pmatrix} \ , \quad \mathbf{G}^B(\mathbf{U}, \mathbf{B}^B) = \begin{pmatrix} -u_x B_y + u_y B_x \\ 0 \end{pmatrix} \ . \tag{3.5}$$

The numerical solutions to $\mathbf{U}$ and $\mathbf{B}^B$ on grid $\mathcal{T}_h$ are denoted as $\mathbf{U}^n_{\mathcal{T}_h} \equiv \mathbf{U}_{\mathcal{T}_h}(\mathbf{x}, t^n)$ and $\mathbf{B}^n_{\mathcal{T}_h} \equiv \mathbf{B}_{\mathcal{T}_h}(\mathbf{x}, t^n)$ at the time $t = t^n$ respectively, where $\mathbf{x} = (x, y)$. On grid $\mathcal{W}_h$, only the x- and y-component of the magnetic induction equation, namely, Eq. (3.4) is solved. The approximate solution to $\mathbf{B}^B$ on $\mathcal{W}_h$ is denoted as $\mathbf{B}^n_{\mathcal{W}_h} \equiv \mathbf{B}_{\mathcal{W}_h}(\mathbf{x}, t^n)$.

The following discrete space is used for approximating $\mathbf{U}$ on the grid $\mathcal{T}_h$:

$$\boldsymbol{\mathcal{U}}_{\mathcal{T}_h} = \left\{ \mathbf{v} \in \left[L^2(\Omega)\right]^6 : \mathbf{v}|_{\mathcal{K}_i} \in \left[P^q(\mathcal{K}_i)\right]^6, \forall \mathcal{K}_i \in \mathcal{T}_h \right\} , \tag{3.6}$$

where $P^q(\mathcal{K}_i)$ represents the space of polynomials of degrees no more than q supported on cell $\mathcal{K}_i$.

We introduce the following divergence-free vector space for approximating $\mathbf{B}^B$ on both $\mathcal{T}_h$ and $\mathcal{W}_h$:

$$\begin{aligned} \boldsymbol{\mathcal{B}}_{\mathcal{T}_h} = & \left\{ \mathbf{v} \in H(\mathrm{div}^0; \Omega) : \mathbf{v}|_{\mathcal{K}_i} \in \left[P^q(\mathcal{K}_i)\right]^2, \forall \mathcal{K}_i \in \mathcal{T}_h \right\} \\ = & \left\{ \mathbf{v} : \mathbf{v}|_{\mathcal{K}_i} \in \boldsymbol{\Pi}^q(\mathcal{K}_i), \text{ and the normal component of } \mathbf{v} \right. \\ & \left. \text{ is continuous across } \partial\mathcal{K}_i, \forall \mathcal{K}_i \in \mathcal{T}_h \right\} , \\ \boldsymbol{\mathcal{B}}_{\mathcal{W}_h} = & \left\{ \mathbf{v} \in H(\mathrm{div}^0; \Omega) : \mathbf{v}|_{T_{s,i}} \in \left[P^q(T_{s,i})\right]^2, \forall \text{ partial cell } T_{s,i} \in \mathcal{D}_i, \forall \mathcal{D}_i \in \mathcal{W}_h \right\} , \end{aligned} \tag{3.7}$$

$$\begin{aligned} & H(\mathrm{div}^0; \Omega) = \left\{ \mathbf{v} \in H(\mathrm{div}; \Omega) : \nabla \cdot \mathbf{v} = 0 \right\} , \\ & H(\mathrm{div}; \Omega) = \left\{ \mathbf{v} \in \left[L^2(\Omega)\right]^2 : \nabla \cdot \mathbf{v} \in L^2(\Omega) \right\} , \\ & \boldsymbol{\Pi}^q(\mathcal{C}) = \left\{ \mathbf{v} \in \left[P^q(\mathcal{C})\right]^2, \nabla \cdot \mathbf{v}|_{\mathcal{C}} = 0, \mathcal{C} \text{ is a cell in } \mathcal{T}_h \text{ or a partial cell in } \mathcal{W}_h \right\} . \end{aligned} \tag{3.8}$$

The numerical solutions $\mathbf{B}^n_{\mathcal{W}_h} \in \boldsymbol{\mathcal{B}}_{\mathcal{W}_h}$ and $\mathbf{B}^n_{\mathcal{T}_h} \in \boldsymbol{\mathcal{B}}_{\mathcal{T}_h}$ at the time $t = t^n$.

We also define the following locally divergence-free vector space on grid $\mathcal{T}_h$:

$$\boldsymbol{\mathcal{B}}_{\mathcal{T}_h, loc} = \left\{ \mathbf{v} : \mathbf{v}|_{\mathcal{K}_i} \in \boldsymbol{\Pi}^q(\mathcal{K}_i), \forall \mathcal{K}_i \in \mathcal{T}_h \right\} . \tag{3.9}$$

In each time step, the new central DG scheme uses a **computation** and a **reconstruction** sub-step to compute the approximate solutions to Eqs. (3.2) and (3.4), and they are detailed in Alg. 1.

Algorithm 1: Numerical Algorithm of the Central DG Scheme

- **Computation** sub-step: suppose $\mathbf{U}^n_{\mathcal{T}_h}$, $\mathbf{B}^n_{\mathcal{W}_h}$ and $\mathbf{B}^n_{\mathcal{T}_h}$ are given.
  1. Compute $\mathbf{U}^{n+1}_{\mathcal{T}_h} \in \boldsymbol{\mathcal{U}}_{\mathcal{T}_h}$ and $\mathbf{B}^{n+1}_{\mathcal{T}_h,loc} \in \boldsymbol{\mathcal{B}}_{\mathcal{T}_h,loc}$ supported on grid cells of $\mathcal{T}_h$.
  2. Compute $b^{n+1}_{\mathcal{W}_h}$ supported on grid edges of $\mathcal{W}_h$.
- **Reconstruction** sub-step: suppose $b^{n+1}_{\mathcal{W}_h}$, $\mathbf{U}^{n+1}_{\mathcal{T}_h}$ and $\mathbf{B}^{n+1}_{\mathcal{T}_h,loc}$ are given.
  1. Limit $\mathbf{U}^{n+1}_{\mathcal{T}_h}$ and $\mathbf{B}^{n+1}_{\mathcal{T}_h,loc}$ if necessary when solving shock wave problems.
  2. Limit $b^{n+1}_{\mathcal{W}_h}$ if necessary when solving shock wave problems.
  3. Reconstruct $\mathbf{B}^{n+1}_{\mathcal{W}_h} \in \boldsymbol{\mathcal{B}}_{\mathcal{W}_h}$ on grid cells of $\mathcal{W}_h$ by using $b^{n+1}_{\mathcal{W}_h}$ and $\mathbf{B}^{n+1}_{\mathcal{T}_h,loc}$.
  4. Reconstruct $\mathbf{B}^{n+1}_{\mathcal{T}_h} \in \boldsymbol{\mathcal{B}}_{\mathcal{W}_h}$ on grid cells of $\mathcal{T}_h$ by using $\mathbf{B}^{n+1}_{\mathcal{W}_h}$.

$b^{n+1}_{\mathcal{W}_h}$ is the numerical solution of the normal component of the magnetic field supported on grid edges of $\mathcal{W}_h$ at time $t = t^{n+1}$.

Implementation of these sub-steps is described in the following subsections.

3.1 Updating $\mathbf{U}^{n+1}_{\mathcal{T}_h}$ on $\mathcal{T}_h$

Given the approximate solution $\mathbf{U}^n_{\mathcal{T}_h}$ supported on grid $\mathcal{T}_h$, and $\mathbf{B}^n_{\mathcal{W}_h}$ supported on grid $\mathcal{W}_h$, we proceed to compute the approximate solution $\mathbf{U}^{n+1}_{\mathcal{T}_h} \in \boldsymbol{\mathcal{U}}_{\mathcal{T}_h}$ of Eq. (3.2) at the next time level, $t^{n+1} = \triangle t^n + t^n$ by using a DG scheme with a numerical flux function utilizing information from solutions defined on both grids.

Let $U^{(i)}_{h,k}(\mathbf{x}, t)$ denote the k^{th} $(k = 1, \ldots, 6)$ component of the approximate solution $\mathbf{U}_{\mathcal{T}_h}(\mathbf{x}, t)$ to Eq. (3.2) restricted on cell $\mathcal{K}_i$. We use the following basis function set for representing $U^{(i)}_{h,k}(\mathbf{x}, t)$:

$$\begin{aligned}\left\{\phi^{(i)}_m(\mathbf{x}) : m = 0, \ldots, r\right\} \equiv \Bigg\{ & 1, \tfrac{(x-x_i)}{\sqrt{|\mathcal{K}_i|}}, \tfrac{(y-y_i)}{\sqrt{|\mathcal{K}_i|}}, \tfrac{(x-x_i)^2}{(\sqrt{|\mathcal{K}_i|})^2}, \\ & \tfrac{(x-x_i)(y-y_i)}{(\sqrt{|\mathcal{K}_i|})^2}, \tfrac{(y-y_i)^2}{(\sqrt{|\mathcal{K}_i|})^2}, \ldots, \tfrac{(y-y_i)^q}{(\sqrt{|\mathcal{K}_i|})^q} \Bigg\} ,\end{aligned} \tag{3.10}$$

where $\mathbf{x}_i \equiv (x_i, y_i)$ is the centroid of $\mathcal{K}_i$, $r = (q+1)(q+2)/2 - 1$ and $|\mathcal{K}_i|$ is the area of cell $\mathcal{K}_i$. These are monomials of the 2D Taylor expansion about the cell centroid (x_i, y_i), scaled by the area of the cell raised to proper powers. In this paper, we only consider the case of $q = 1$.

$U^{(i)}_{h,k}(\mathbf{x}, t)$ then is represented by

$$U^{(i)}_{h,k}(\mathbf{x}, t) = \sum_{m=0}^{r} \hat{U}^{(i)}_{m,k}(t)\phi^{(i)}_m(\mathbf{x}) \ . \tag{3.11}$$

The semi-discrete DG scheme for solving each component of Eq. (3.2) to obtain $\mathbf{U}^{n+1}_{\mathcal{T}_h}$ is formulated as: For each $k = 1, \ldots, 6$ and $\forall \mathcal{K}_i \in \mathcal{T}_h$, find $U^{(i)}_{h,k}(\mathbf{x}, t)$ such that for every

$\phi_m^{(i)}, m = 0, \ldots, r,$

$$\begin{aligned}&\frac{d}{dt}\int_{\mathcal{K}_i} U_{h,k}^{(i)}(\mathbf{x},t)\phi_m^{(i)} d\mathbf{x} = \\ &\quad -\sum_{e\in\partial\mathcal{K}_i}\int_e h_{e,k}(\mathbf{x},t)\phi_m^{(i)} d\Gamma + \int_{\mathcal{K}_i}\left(F_k(\mathbf{U}_{\mathcal{T}_h},\mathbf{B}_{\mathcal{W}_h}), G_k(\mathbf{U}_{\mathcal{T}_h},\mathbf{B}_{\mathcal{W}_h})\right)\cdot\nabla\phi_m^{(i)} d\mathbf{x}\ ,\end{aligned} \tag{3.12}$$

where F_k and G_k are the k^{th} component of fluxes $\mathbf{F}$ and $\mathbf{G}$, respectively, e is any edge of $\mathcal{K}_i$. It is important to note that $\mathbf{B}_{\mathcal{W}_h}$ is the magnetic field solution defined on grid $\mathcal{W}_h$ (the idea of the central DG scheme on overlapping cells is adopted here). Let $\boldsymbol{\nu}_{e,i}$ be the outward unit normal of edge e of cell $\mathcal{K}_i$, and $h_{e,k}$ be the numerical flux function. In this paper, $h_{e,k}$ is the Lax-Friedrich flux function which reads:

$$\begin{aligned}&h_{e,k}(\mathbf{x},t) = \\ &\tfrac{1}{2}\Big[\ \left(F_k\left(\mathbf{U}_{\mathcal{T}_h,in},\mathbf{B}_{\mathcal{W}_h}\right), G_k\left(\mathbf{U}_{\mathcal{T}_h,in},\mathbf{B}_{\mathcal{W}_h}\right)\right) + \left(F_k\left(\mathbf{U}_{\mathcal{T}_h,out},\mathbf{B}_{\mathcal{W}_h}\right), G_k\left(\mathbf{U}_{\mathcal{T}_h,out},\mathbf{B}_{\mathcal{W}_h}\right)\right)\ \Big]\cdot\boldsymbol{\nu}_{e,i} \\ &+\tfrac{\alpha}{2}\left(U_{h,k,in} - U_{h,k,out}\right)\ ,\end{aligned} \tag{3.13}$$

where $\alpha = \max(|\mathbf{u}| + c)$. c is the speed of the fast magneto-acoustic wave [6]. The k^{th} components of $\mathbf{U}_{\mathcal{T}_h,in}$ and $\mathbf{U}_{\mathcal{T}_h,out}$ are defined by

$$U_{h,k,in}(\mathbf{x},t) = \lim_{\mathbf{y}\to\mathbf{x},\mathbf{y}\in\mathcal{K}_i^{\text{int}}} U_{h,k}^{(i)}(\mathbf{y},t)\ , \tag{3.14}$$

$$U_{h,k,out}(\mathbf{x},t) = \lim_{\mathbf{y}\to\mathbf{x},\mathbf{y}\notin\overline{\mathcal{K}_i}} U_{h,k}^{(i)}(\mathbf{y},t)\ , \tag{3.15}$$

and $\mathcal{K}_i^{\text{int}}$ indicates the interior of cell $\mathcal{K}_i$.

The forward Euler time discretization for discretizing Eq. (3.12) is: For each $k = 1, \ldots, 6$ and $\forall\mathcal{K}_i \in \mathcal{T}_h$, find $U_{h,k}^{(i)}(\mathbf{x}, t^{n+1})$ such that for every $\phi_m^{(i)}, m = 0, \ldots, r,$

$$\begin{aligned}&\int_{\mathcal{K}_i} U_{h,k}^{(i)}(\mathbf{x},t^{n+1})\phi_m^{(i)} d\mathbf{x} - \int_{\mathcal{K}_i} U_{h,k}^{(i)}(\mathbf{x},t^n)\phi_m^{(i)} d\mathbf{x} = \\ &\quad -\triangle t^n\sum_{e\in\partial\mathcal{K}_i}\int_e h_{e,k}(\mathbf{x},t^n)\phi_m^{(i)} d\Gamma + \triangle t^n\int_{\mathcal{K}_i}\left(F_k(\mathbf{U}_{\mathcal{T}_h}^n,\mathbf{B}_{\mathcal{W}_h}^n), G_k(\mathbf{U}_{\mathcal{T}_h}^n,\mathbf{B}_{\mathcal{W}_h}^n)\right)\cdot\nabla\phi_m^{(i)} d\mathbf{x}\ .\end{aligned} \tag{3.16}$$

Integrals in Eq. (3.16) are evaluated by appropriate Gaussian quadrature rules [5].

The divergence-free $\mathbf{B}_{\mathcal{T}_h}$ could also be used in (3.12) as in conventional CT schemes on non-staggered grids. In this paper the divergence free $\mathbf{B}_{\mathcal{W}_h}$ is firstly computed through a central scheme followed by a CT reconstruction on the dual mesh, then the divergence-free $\mathbf{B}_{\mathcal{T}_h}$ is computed on the triangular mesh from $\mathbf{B}_{\mathcal{W}_h}$. Therefore $\mathbf{B}_{\mathcal{T}_h}$ should contain larger error than $\mathbf{B}_{\mathcal{W}_h}$. Also $\mathbf{B}_{\mathcal{W}_h}$ is continuous across cell edges of a triangular cell while $\mathbf{B}_{\mathcal{T}_h}$ isn't (only its normal component is), which makes the computation of fluxes in Eq. (3.12) easier. Numerical tests also show that $U_{h,k}^{(i)}(\mathbf{x}, t^{n+1})$ computed with using $\mathbf{B}_{\mathcal{T}_h}$ in flux evaluation has error larger than that computed with using $\mathbf{B}_{\mathcal{W}_h}$ in flux evaluation.

3.2 Updating $\mathbf{B}_{\mathcal{T}_h,loc}^{n+1}$ on $\mathcal{T}_h$

Given $\mathbf{B}_{\mathcal{T}_h}^n$ and $\mathbf{U}_{\mathcal{T}_h}^n$ supported on grid $\mathcal{T}_h$ and $\mathbf{B}_{\mathcal{W}_h}^n$ supported on grid $\mathcal{W}_h$, the approximate solution $\mathbf{B}_{\mathcal{T}_h,loc}^{n+1} \in \boldsymbol{\mathcal{B}}_{\mathcal{T}_h,loc}$ to Eq. (3.4) at the next time level $t^{n+1} = \triangle t^n + t^n$ is computed.

This solution will be used to help reconstruct globally divergence-free magnetic field $\mathbf{B}_{\mathcal{W}_h}^{n+1}$ on the dual grid $\mathcal{W}_h$.

We modify the central DG scheme on overlapping cells to compute $\mathbf{B}_{\mathcal{T}_h,loc}^{n+1}$. Details of the modification are given as follows.

When $q = 1$, the following basis is used to span the local space $\mathbf{\Pi}^q(\mathcal{K}_i)$ for $\mathbf{B}_{\mathcal{T}_h,loc}(\mathbf{x},t)$ restricted on cell $\mathcal{K}_i$:

$$\left\{\boldsymbol{\psi}_s^{(i)}(\mathbf{x}), s = 0,\ldots,4\right\} \equiv \left\{ \begin{pmatrix} 1 \\ 0 \end{pmatrix}, \begin{pmatrix} 0 \\ 1 \end{pmatrix}, \begin{pmatrix} \frac{x-x_i}{\sqrt{|\mathcal{K}_i|}} \\ -\frac{y-y_i}{\sqrt{|\mathcal{K}_i|}} \end{pmatrix}, \begin{pmatrix} \frac{y-y_i}{\sqrt{|\mathcal{K}_i|}} \\ 0 \end{pmatrix}, \begin{pmatrix} 0 \\ \frac{x-x_i}{\sqrt{|\mathcal{K}_i|}} \end{pmatrix} \right\} . \tag{3.17}$$

Let's use $\mathbf{B}_{\mathcal{T}_h,loc}^{(i)}(\mathbf{x},t)$ to denote the locally divergence-free solution to Eq. (3.4) supported on $\mathcal{K}_i$. $\mathbf{B}_{\mathcal{T}_h,loc}^{(i)}(\mathbf{x},t)$ is represented by:

$$\mathbf{B}_{\mathcal{T}_h,loc}^{(i)}(\mathbf{x},t) = \sum_{s=0}^{4} \hat{B}_s^{(i)}(t)\boldsymbol{\psi}_s^{(i)}(\mathbf{x}) . \tag{3.18}$$

The semi-discrete modified central DG scheme to solve Eq. (3.4) to obtain $\mathbf{B}_{\mathcal{T}_h,loc}^{n+1}$ is formulated as: $\forall \mathcal{K}_i \in \mathcal{T}_h$, find $\mathbf{B}_{\mathcal{T}_h,loc}^{(i)}(\mathbf{x},t) \in \mathbf{\Pi}^q(\mathcal{K}_i)$ such that for every $\boldsymbol{\psi}_s^{(i)}, s = 0,\ldots,4$,

$$\begin{aligned} \frac{d}{dt}\int_{\mathcal{K}_i} \mathbf{B}_{\mathcal{T}_h,loc}^{(i)}(\mathbf{x},t)\cdot\boldsymbol{\psi}_s^{(i)} d\mathbf{x}\,\Big|_{t=t^n} &= \frac{1}{\Delta\tau^n}\int_{\mathcal{K}_i}\left(\mathbf{B}_{\mathcal{W}_h}^n - \mathbf{B}_{\mathcal{T}_h}^n\right)\cdot\boldsymbol{\psi}_s^{(i)} d\mathbf{x} \\ &- \sum_{e\in\partial\mathcal{K}_i}\int_e \boldsymbol{\psi}_s^{(i)}\cdot\left(\left(\mathbf{F}^B(\mathbf{U}_{\mathcal{T}_h}^n,\mathbf{B}_{\mathcal{W}_h}^n),\mathbf{G}^B(\mathbf{U}_{\mathcal{T}_h}^n,\mathbf{B}_{\mathcal{W}_h}^n)\right)\cdot\boldsymbol{\nu}_{e,i}\right) d\Gamma \\ &+ \int_{\mathcal{K}_i}\left(\mathbf{F}^B(\mathbf{U}_{\mathcal{T}_h}^n,\mathbf{B}_{\mathcal{W}_h}^n),\mathbf{G}^B(\mathbf{U}_{\mathcal{T}_h}^n,\mathbf{B}_{\mathcal{W}_h}^n)\right)\cdot\nabla\boldsymbol{\psi}_s^{(i)} d\mathbf{x} , \end{aligned} \tag{3.19}$$

where $\Delta\tau^n$ is the upper bound for the time step size due to the CFL restriction at t^n. Notice that the initial value used to solve Eq. (3.19) is $\mathbf{B}_{\mathcal{T}_h}^n$, which is globally divergence-free.

For example, when the forward Euler time discretization is employed to discretize Eq. (3.19), the fully discrete scheme reads as: $\forall \mathcal{K}_i \in \mathcal{T}_h$, find $\mathbf{B}_{\mathcal{T}_h,loc}^{(i)}(\mathbf{x},t^{n+1}) \in \mathbf{\Pi}^q(\mathcal{K}_i)$ such that for every $\boldsymbol{\psi}_s^{(i)}, s = 0,\ldots,4$,

$$\begin{aligned} \int_{\mathcal{K}_i} \mathbf{B}_{\mathcal{T}_h,loc}^{(i)}(\mathbf{x},t^{n+1})\cdot\boldsymbol{\psi}_s^{(i)} d\mathbf{x} - \int_{\mathcal{K}_i} \mathbf{B}_{\mathcal{T}_h}^{(i)}(\mathbf{x},t^n)\cdot\boldsymbol{\psi}_s^{(i)} d\mathbf{x} &= \frac{\triangle t^n}{\Delta\tau^n}\int_{\mathcal{K}_i}\left(\mathbf{B}_{\mathcal{W}_h}^n - \mathbf{B}_{\mathcal{T}_h}^n\right)\cdot\boldsymbol{\psi}_s^{(i)} d\mathbf{x} \\ &- \triangle t^n \sum_{e\in\partial\mathcal{K}_i}\int_e \boldsymbol{\psi}_s^{(i)}\cdot\left(\left(\mathbf{F}^B(\mathbf{U}_{\mathcal{T}_h}^n,\mathbf{B}_{\mathcal{W}_h}^n),\mathbf{G}^B(\mathbf{U}_{\mathcal{T}_h}^n,\mathbf{B}_{\mathcal{W}_h}^n)\right)\cdot\boldsymbol{\nu}_{e,i}\right) d\Gamma \\ &+ \triangle t^n\int_{\mathcal{K}_i}\left(\mathbf{F}^B(\mathbf{U}_{\mathcal{T}_h}^n,\mathbf{B}_{\mathcal{W}_h}^n),\mathbf{G}^B(\mathbf{U}_{\mathcal{T}_h}^n,\mathbf{B}_{\mathcal{W}_h}^n)\right)\cdot\nabla\boldsymbol{\psi}_s^{(i)} d\mathbf{x} . \end{aligned} \tag{3.20}$$

Eq. (3.19) is a central DG scheme on overlapping cells ([16, 17]) taking advantage of the presence of $\mathbf{B}_{\mathcal{W}_h}^n$ on the dual mesh. The role of the term with $\mathbf{B}_{\mathcal{W}_h}^n - \mathbf{B}_{\mathcal{T}_h}^n$ is to provide sufficient amount of diffusion to stabilize the computation of $\mathbf{B}_{\mathcal{T}_h,loc}^{(i)}$, similar to the role of the diffusive term in a Lax-Friedrichs flux (see e.g. [38]). One could also update the magnetic

field on the triangular mesh directly without using $\mathbf{B}^n_{\mathcal{W}_h}$, see [12]. Note that in Eqs. (3.19) and (3.20), $\mathbf{U}^n_{\mathcal{T}_h}$ defined on the primal grid is used to evaluate the flux function because $\mathbf{U}^n_{\mathcal{T}_h}$ is only supported on grid $\mathcal{T}_h$. Since $\mathbf{U}^n_{\mathcal{T}_h}$ is not continuous across cell edges, an arithmetic average of the jump values of the fluxes is used (which is also the Lax-Friedrichs flux because $\mathbf{B}^n_{\mathcal{W}_h}$ is continuous here).

3.3 Updating $b^{n+1}_{\mathcal{W}_h}$ on $\mathcal{W}_h$

In this sub-section, the central DG scheme in combination with the CT framework is designated to compute the approximate solution $b^{n+1}_{\mathcal{W}_h}$, the normal component of the magnetic field defined on each of the grid edges of $\mathcal{W}_h$ at the time level t^{n+1}. Note that the numerical magnetic field is globally divergence-free if and only if the normal component of the numerical magnetic field is continuous across the element interfaces. Therefore, we first compute $b^{n+1}_{\mathcal{W}_h}$, and then reconstruct $\mathbf{B}^{n+1}_{\mathcal{W}_h}$ element-by-element on all $\mathcal{D}_j \in \mathcal{W}_h$ so that $\nabla \cdot \mathbf{B}^{n+1}_{\mathcal{W}_h} = 0$ in the interior of partial cells of $\mathcal{D}_j$ and the normal component of $\mathbf{B}^{n+1}_{\mathcal{W}_h}$ defined on the interfaces of $\mathcal{D}_j$ matches with $b^{n+1}_{\mathcal{W}_h}$ supported on $\mathcal{D}_j$ interfaces exactly. Moreover, the normal component of $\mathbf{B}^{n+1}_{\mathcal{W}_h}$ is continuous across interfaces of partial cells.

Denote $\mathcal{L}_h = \{e^{\mathcal{W}}_\jmath, \jmath = 1, \ldots, \mathcal{N}_e\}$ the set of grid edges of the dual grid $\mathcal{W}_h$. $e^{\mathcal{W}}_\jmath$ connects centroids of triangular cells of $\mathcal{T}_h$. Let the unit edge normal of the edge $e^{\mathcal{W}}_\jmath$ be $\boldsymbol{\nu}^{\mathcal{W}}_\jmath$ and tangent be $\boldsymbol{\zeta}^{\mathcal{W}}_\jmath$. $\boldsymbol{\zeta}^{\mathcal{W}}_\jmath$ is obtained by rotating $\boldsymbol{\nu}^{\mathcal{W}}_\jmath$ 90 degrees in the counterclockwise direction.

On each $e^{\mathcal{W}}_\jmath$, we rewrite Eq. (3.4) by contributions of $\mathbf{B}^B$ in the directions of $\boldsymbol{\nu}^{\mathcal{W}}_\jmath$ and $\boldsymbol{\zeta}^{\mathcal{W}}_\jmath$ to obtain

$$\partial_t \begin{pmatrix} b_{\nu_\jmath \mathcal{W}} \\ b_{\zeta_\jmath \mathcal{W}} \end{pmatrix} + \partial_{\nu_\jmath} \begin{pmatrix} 0 \\ u_{\nu_\jmath} b_{\zeta_\jmath \mathcal{W}} - u_{\zeta_\jmath} b_{\nu_\jmath \mathcal{W}} \end{pmatrix} + \partial_{\zeta_\jmath} \begin{pmatrix} -u_{\nu_\jmath} b_{\zeta_\jmath \mathcal{W}} + u_{\zeta_\jmath} b_{\nu_\jmath \mathcal{W}} \\ 0 \end{pmatrix} = \mathbf{0} \ , \tag{3.21}$$

where $b_{\nu_\jmath \mathcal{W}} = \mathbf{B}^B \cdot \boldsymbol{\nu}^{\mathcal{W}}_\jmath$, $b_{\zeta_\jmath \mathcal{W}} = \mathbf{B}^B \cdot \boldsymbol{\zeta}^{\mathcal{W}}_\jmath$, and $u_{\nu_\jmath}$ and $u_{\zeta_\jmath}$ are the components of the velocity $\mathbf{u}$ in the $\boldsymbol{\nu}^{\mathcal{W}}_\jmath$ and $\boldsymbol{\zeta}^{\mathcal{W}}_\jmath$ directions, respectively. $(\nu_\jmath, \zeta_\jmath)$ is the coordinate in the $\left(\boldsymbol{\nu}^{\mathcal{W}}_\jmath, \boldsymbol{\zeta}^{\mathcal{W}}_\jmath\right)$ coordinate system.

Along the $\boldsymbol{\zeta}^{\mathcal{W}}_\jmath$ direction, let $\mathbf{x}_{0,\jmath}$ and $\mathbf{x}_{1,\jmath}$ be the starting and ending points of edge $e^{\mathcal{W}}_\jmath$ which is parametrized by

$$\mathbf{x}(\hat{\zeta}_\jmath) = \frac{\mathbf{x}_{0,\jmath} + \mathbf{x}_{1,\jmath}}{2} + \frac{\mathbf{x}_{1,\jmath} - \mathbf{x}_{0,\jmath}}{2} \hat{\zeta}_\jmath \ , \quad \hat{\zeta}_\jmath \in [-1, 1] \ . \tag{3.22}$$

With this affine mapping we can consider the first equation of (3.21) on a reference spatial coordinate of $\hat{\zeta}_\jmath \in [-1, 1]$. Denote $b^{(\jmath)}_h(\cdot, t)$ the numerical approximation to $b_{\nu_\jmath \mathcal{W}}(\cdot, t)$ supported on edge $e^{\mathcal{W}}_\jmath$. The basis used to span the polynomial space $P^q\left(\hat{\zeta}_\jmath\right)$ $(q = 1)$ for representing $b^{(\jmath)}_h$ is

$$\left\{\varphi_s(\hat{\zeta}_\jmath), s = 0, 1\right\} \equiv \left\{1, \hat{\zeta}_\jmath\right\} \ . \tag{3.23}$$

Let

$$b^{(\jmath)}_h(\hat{\zeta}_\jmath, t) = \sum_{s=0}^{1} \hat{b}^{(\jmath)}_s(t) \varphi_s(\hat{\zeta}_\jmath) \ . \tag{3.24}$$

The first equation of (3.21) is solved by the central DG scheme on overlapping cells. Computations are performed using an affine transformation which maps integrals over $e_j^{\mathcal{W}}$ to integrals with respect to $\hat{\zeta}_j \in [-1,1]$ on which the basis functions are defined. The semi-discrete central DG method for computing $b_{h,}^{(j)}(\hat{\zeta}_j, t^{n+1})$ is formulated as follows:

$\forall e_j^{\mathcal{W}} \in \mathcal{L}_h$, find $b_{h,}^{(j)}(\hat{\zeta}_j, t)$, a linear polynomial in $\hat{\zeta}_j \in [-1,1]$, such that for any $\varphi_s(\hat{\zeta}_j), s = 0, 1,$

$$\begin{aligned} \frac{d}{dt}\int_{-1}^{1} b_h^{(j)}\varphi_s d\hat{\zeta}_j \Big|_{t=t^n} &= \frac{1}{\Delta\tau^n}\int_{-1}^{1}\left(b_{\mathcal{T}_h}^{(j)}(t^n) - b_h^{(j)}(t^n)\right)\varphi_s d\hat{\zeta}_j \\ &\quad - \frac{2}{\mid e_j^{\mathcal{W}} \mid}\left[E_{z,\mathcal{T}_h}(\hat{\zeta}_j)\varphi_s \Big|_{-1}^{1} - \int_{-1}^{1} E_{z,\mathcal{T}_h}(\hat{\zeta}_j)\frac{d\varphi_s}{d\hat{\zeta}_j}d\hat{\zeta}_j\right] , \end{aligned} \tag{3.25}$$

where $b_{\mathcal{T}_h}^{(j)}(t^n)$ is $\mathbf{B}_{\mathcal{T}_h}^n \cdot \boldsymbol{\nu}_j$ restricted on edge $e_j^{\mathcal{W}}$, $E_{z,\mathcal{T}_h}$ is the z-component of the electric field $\mathbf{E}$ defined on $\mathcal{T}_h$, and $\mid e_j^{\mathcal{W}} \mid$ is the length of edge $e_j^{\mathcal{W}}$. As before, Eq. (3.25) can be discretized by the forward Euler time discretization as a component of the TVD Runge-Kutta method.

By letting $\varphi_s = 1$ in Eq. (3.25), it is easy to verify that $b_{h,}^{(j)}(\hat{\zeta}_j, t^{n+1})$ satisfies the following compatibility condition

$$\int_{\partial\mathcal{D}_j} b_h^{(j)}(t^{n+1})d\hat{\zeta} = 0 \ , \quad \forall \mathcal{D}_j \in \mathcal{W}_h \text{ and } b_h^{(j)}(t^{n+1}) \text{ is supported on } \partial\mathcal{D}_{\mathrm{j}} \ , \tag{3.26}$$

provided $\mathbf{B}_{\mathcal{T}_h}^n$ and $\mathbf{B}_{\mathcal{W}_h}^n$ is globally divergence-free.

With this compatibility condition, we proceed to do element-by-element divergence-free reconstruction to obtain $\mathbf{B}_{\mathcal{W}_h}^{n+1}$. The reconstruction algorithm is described in the following sub-section.

3.4 Reconstructing exactly divergence-free $\mathbf{B}_{\mathcal{W}_h}^{n+1}$ on $\mathcal{W}_h$

An algorithm to reconstruct a piecewise linear and globally divergence-free magnetic field $\mathbf{B}_{\mathcal{W}_h}^{n+1}$ on $\mathcal{W}_h$ is discussed in this section. The reconstructed $\mathbf{B}_{\mathcal{W}_h}^{n+1}$ satisfies the divergence-free condition in the interior of any partial cell. The normal component of the reconstructed $\mathbf{B}_{\mathcal{W}_h}^{n+1}$ is continuous across cell edges of partial cells and dual cells, and also retains consistency at the boundary of a dual cell, namely, $\left(\mathbf{B}_{\mathcal{W}_h}^{n+1} \cdot \boldsymbol{\nu}_j^{\mathcal{W}}\right)\Big|_{e_j^{\mathcal{W}}} = b_h^{(j)}(\cdot, t^{n+1})$.

The reconstruction is a local process and proceeds dual cell-by-dual cell. Consider to reconstruct $\mathbf{B}_{\mathcal{W}_h}^{n+1}$ on dual cell $\mathcal{D}_1$, as shown in Fig. 1. On each of its partial cell $T_{\ell,1}$, $\ell = 1, \ldots, 6$, let $(B_{x,T_{\ell,1}}, B_{y,T_{\ell,1}})^t$ denote the reconstructed magnetic field restricted on $T_{\ell,1}$ at time t^{n+1}, i.e.,

$$(B_{x,T_{\ell,1}}, B_{y,T_{\ell,1}})^t = \mathbf{B}_{\mathcal{W}_h}^{n+1}\chi_{T_{\ell,1}}(x,y) \ . \tag{3.27}$$

Note that $\mathcal{D}_1 = \bigcup_{\ell=1}^{6} T_{\ell,1}$, and $\chi_{T_{\ell,1}}(x,y)$ is the characteristic function supported on partial cell $T_{\ell,1}$. $(B_{x,T_{\ell,1}}, B_{y,T_{\ell,1}})^t$ is represented by the following form in the present paper

$$\begin{cases} B_{x,T_{\ell,1}}(x,y) = a_{0,T_{\ell,1}} + a_{1,T_{\ell,1}}x + a_{2,T_{\ell,1}}y \\ B_{y,T_{\ell,1}}(x,y) = b_{0,T_{\ell,1}} + b_{1,T_{\ell,1}}x + b_{2,T_{\ell,1}}y \end{cases} , \tag{3.28}$$

and 36 conditions are needed to determine uniquely $(B_{x,T_{\ell,1}}, B_{y,T_{\ell,1}})^t$ for $\ell = 1, \ldots, 6$.

The divergence-free condition, namely, $\nabla \cdot (B_{x,T_{\ell,1}}, B_{y,T_{\ell,1}}) = 0$, leads to the following equation:

$$a_{1,T_{\ell,1}} = -b_{2,T_{\ell,1}} \ , \qquad \ell = 1, \ldots, 6. \tag{3.29}$$

This eliminates six unknown coefficients, or reduces one degree of freedom in reconstructing each $(B_{x,T_{\ell,1}}, B_{y,T_{\ell,1}})^t$.

Let the edge of partial cell $T_{\ell,1}$ connecting two adjacent vertices of $\mathcal{D}_1$ be $e_j^{\mathcal{W}}$. $e_j^{\mathcal{W}}$ is actually in the edge set $\mathcal{L}_h$ of the dual grid $\mathcal{W}_h$. See Fig. 1 for example. $T_{1,1}$'s edge connecting $V1$ and $V2$, $T_{2,1}$'s edge connecting $V2$ and $V3$ and so on are this type of edges. On $e_j^{\mathcal{W}}$, $(B_{x,T_\ell}, B_{y,T_\ell})^t$ needs to satisfy

$$(B_{x,T_{\ell,1}}, B_{y,T_{\ell,1}}) \cdot \boldsymbol{\nu}_j^{\mathcal{W}} = b_h^{(j)}\left(\mathbf{x}, t^{n+1}\right) \ , \qquad \ell = 1, \ldots, 6. \tag{3.30}$$

Notice that $b_h^{(j)}\left(\mathbf{x}, t^{n+1}\right)$ is computed by the scheme presented in sub-section 3.3.

Let $T_{\ell,1}$ and $T_{\ell+1,1}$ be two partial cells belonging to the same dual cell $\mathcal{D}_1$ and be edge adjacent neighbors. Use $e_\ell^{\mathcal{D}_1}$ to denote the edge shared by partial cells $T_{\ell,1}$ and $T_{\ell+1,1}$. See Fig. 1 for example. $e_\ell^{\mathcal{D}_1}$ consists of edges connecting O and $V1$, O and $V2$, ..., and O and $V6$. Let the unit edge normal of $e_\ell^{\mathcal{D}_1}$ be $\boldsymbol{\nu}_\ell^{\mathcal{D}_1}$. On each $e_\ell^{\mathcal{D}_1}$ for $\ell = 1, \ldots, 6$, the magnetic field $(B_{x,T_{\ell,1}}, B_{y,T_{\ell,1}})^t$ needs to satisfy:

$$(B_{x,T_{\ell,1}}, B_{y,T_{\ell,1}}) \cdot \boldsymbol{\nu}_\ell^{\mathcal{D}_1} = (B_{x,T_{(\ell+1,1) \bmod 6}}, B_{y,T_{(\ell+1,1) \bmod 6}}) \cdot \boldsymbol{\nu}_\ell^{\mathcal{D}_1} \ , \qquad \ell = 1, \ldots, 6. \tag{3.31}$$

Here "mod" is the modulus operator.

Eqs. (3.30) and (3.31) give 24 conditions in which only 23 of them are linearly independent, which is easy to understand. In fact, conditions (3.29) and (3.31) already imply that the reconstructed magnetic field in dual cell $\mathcal{D}_1$ is divergence-free, which then implies that the net influx of the magnetic field across the boundary of cell $\mathcal{D}_1$ is zero. Therefore one equation of the condition (3.30), which is that the first moment of $b_h^{(j)}\left(\mathbf{x}, t^{n+1}\right)$ is equal to the constant part of $(B_{x,T_{1,1}}, B_{y,T_{1,1}}) \cdot \boldsymbol{\nu}_j^{\mathcal{W}}$ is redundant and can be removed from the constraints.

To reconstruct $(B_{x,T_{\ell,1}}, B_{y,T_{\ell,1}})^t$ for $\ell = 1, \ldots, 6$, yet 36 conditions are needed. The rest conditions are given in the least-squares sense as follows. The reconstructed $(B_{x,T_{\ell,1}}, B_{y,T_{\ell,1}})^t$ is required to be equal to $\mathbf{B}_{\mathcal{T}_h,loc}^{n+1}$ at certain locations on $\mathcal{T}_h$ in the least-squares sense. In this paper, 4 values of $\mathbf{B}_{\mathcal{T}_h,loc}^{n+1}$ at 4 different locations are used for determining $(B_{x,T_{\ell,1}}, B_{y,T_{\ell,1}})^t$. Take $(B_{x,T_{1,1}}, B_{y,T_{1,1}})^t$ supported on $T_{1,1}$ of $\mathcal{D}_1$ in Fig. 1 for example. $\mathbf{B}_{\mathcal{T}_h,loc}^{n+1}(V1)$ and $\mathbf{B}_{\mathcal{T}_h,loc}^{n+1}(V2)$ are used. They are $\mathbf{B}_{\mathcal{T}_h,loc}^{n+1}$ evaluated at vertices $V1$ and $V2$, respectively. Denote the midpoint of the edge connecting O and $V1$ as $M1$ and the midpoint of the edge connecting O and $V2$ as $M2$. $(B_{x,T_{1,1}}, B_{y,T_{1,1}})^t$ also equals to $\mathbf{B}_{\mathcal{T}_h,loc}^{n+1}(M1)$ and $\mathbf{B}_{\mathcal{T}_h,loc}^{n+1}(M2)$ in the least-squares sense, respectively.

Eqs. (3.29), (3.30) and (3.31), together with these least-squares constraints are solved by the linearly constrained least-squares method to determine $(B_{x,T_{\ell,1}}, B_{y,T_{\ell,1}})^t$, for $\ell = 1, \ldots, 6$.

On each dual cell, this reconstruction procedure is applied. Thus a piecewise linear $\mathbf{B}_{\mathcal{W}_h}^{n+1}$ restricted on dual cell $\mathcal{D}_j$ is given by

$$\mathbf{B}_{\mathcal{W}_h}^{n+1}\Big|_{\mathbf{x} \in T_{\ell,j}} = (B_{x,T_{\ell,j}}, B_{y,T_{\ell,j}})^t \ , \qquad T_{\ell,j} \in \mathcal{D}_j, \ j = 1, \ldots, \mathcal{N}_{\mathcal{W}} \ .$$

3.5 Reconstructing exactly divergence-free $\mathbf{B}_{\mathcal{T}_h}^{n+1}$ on $\mathcal{T}_h$

$\mathbf{B}_{\mathcal{T}_h}^{n+1}$ is constructed on the primal triangular mesh out of $\mathbf{B}_{\mathcal{W}_h}^{n+1}$ which is defined on the dual mesh, following a CT strategy. The first step is to obtain a linear polynomial $b_{\mathcal{T}}^{(\hat{\imath}),n+1}$ on each primal cell edge which is a second order approximation to the normal component of $\mathbf{B}_{\mathcal{W}_h}^{n+1}$ on the same edge, and ensure that the average of the linear polynomial is equal to that of the normal component of $\mathbf{B}_{\mathcal{W}_h}^{n+1}$ on the cell edge (therefore, the net flux across edges of a primal triangular cell will be zero). Using the computed linear polynomial $b_{\mathcal{T}}^{(\hat{\imath}),n+1}$ on each primal cell edge as the common normal component (for the two cells sharing the same edge) to construct a piecewise linear $\mathbf{B}_{\mathcal{T}_h}^{n+1}$ on the primal triangular mesh, which is divergence-free wherever it's smooth, $\mathbf{B}_{\mathcal{T}_h}^{n+1}$ will be a second order approximation to $\mathbf{B}_{\mathcal{W}_h}^{n+1}$ and have zero net flux across the boundary of any simply connected sub-domain.

Two steps are taken to reconstruct exactly divergence-free $\mathbf{B}_{\mathcal{T}_h}^{n+1}$. In the first step, $\mathbf{B}_{\mathcal{W}_h}^{n+1}$ is projected onto grid edges of the grid $\mathcal{T}_h$. Denote $\mathcal{L}_h^{\mathcal{T}} = \{e_{\hat{\imath}}^{\mathcal{T}}, \hat{\imath} = 1, \ldots, \mathcal{N}_e^{\mathcal{T}}\}$ the set of grid edges of $\mathcal{T}_h$. Let the unit edge normal and tangent of edge $e_{\hat{\imath}}^{\mathcal{T}}$ be $\boldsymbol{\nu}_{\hat{\imath}}^{\mathcal{T}}$ and $\boldsymbol{\zeta}_{\hat{\imath}}^{\mathcal{T}}$ respectively. $\boldsymbol{\zeta}_{\hat{\imath}}^{\mathcal{T}}$ is obtained by rotating $\boldsymbol{\nu}_{\hat{\imath}}^{\mathcal{T}}$ 90 degrees in the counterclockwise direction.

Let $\mathbf{x}_{0,\hat{\imath}}^{\mathcal{T}}$ and $\mathbf{x}_{1,\hat{\imath}}^{\mathcal{T}}$ be the starting and ending points of edge $e_{\hat{\imath}}^{\mathcal{T}}$ in the $\boldsymbol{\zeta}_{\hat{\imath}}^{\mathcal{T}}$ direction. $e_{\hat{\imath}}^{\mathcal{T}}$ is parametrized by

$$\mathbf{x}^{\mathcal{T}}(\hat{\eta}_{\hat{\imath}}) = \frac{\mathbf{x}_{0,\hat{\imath}}^{\mathcal{T}} + \mathbf{x}_{1,\hat{\imath}}^{\mathcal{T}}}{2} + \frac{\mathbf{x}_{1,\hat{\imath}}^{\mathcal{T}} - \mathbf{x}_{0,\hat{\imath}}^{\mathcal{T}}}{2}\hat{\eta}_{\hat{\imath}} \ , \quad \hat{\eta}_{\hat{\imath}} \in [-1, 1] \ . \tag{3.32}$$

For convenience in discussion, we also use the notation $e_{l,i}^{\mathcal{T}}, l = 1, 2, 3$ to denote edges of $\mathcal{K}_i$.

Denote $b_{\mathcal{T}}^{(\hat{\imath}),n+1}$ the approximate solution to the normal component of $\mathbf{B}^B$ on edge $e_{\hat{\imath}}^{\mathcal{T}}$ at the time level t^{n+1}, $b_{\mathcal{T}}^{(\hat{\imath}),n+1}$ is obtained by L^2 projection of $\mathbf{B}_{\mathcal{W}_h}^{n+1}$ onto $e_{\hat{\imath}}^{\mathcal{T}}$ as follows:

$$\int_{-1}^{1} b_{\mathcal{T}}^{(\hat{\imath}),n+1}\psi \left|\frac{\partial \mathbf{x}^{\mathcal{T}}(\hat{\eta}_{\hat{\imath}})}{\partial \hat{\eta}_{\hat{\imath}}}\right| d\hat{\eta}_{\hat{\imath}} = \int_{-1}^{1} \mathbf{B}_{\mathcal{W}_h}^{n+1}\left(x(\hat{\eta}_{\hat{\imath}}), y(\hat{\eta}_{\hat{\imath}})\right) \cdot \boldsymbol{\nu}_{\hat{\imath}}^{\mathcal{T}} \psi \left|\frac{\partial \mathbf{x}^{\mathcal{T}}(\hat{\eta}_{\hat{\imath}})}{\partial \hat{\eta}_{\hat{\imath}}}\right| d\hat{\eta}_{\hat{\imath}} \ , \forall \psi \in P^1(\hat{\eta}_{\hat{\imath}}) \tag{3.33}$$

A simpler implementation could also be used to obtain $b_{\mathcal{T}}^{(\hat{\imath}),n+1}$. Note that edge $e_{\hat{\imath}}^{\mathcal{T}}$ passes through two dual cells. See Fig. 1 for example. The first moment of $b_{\mathcal{T}}^{(\hat{\imath}),n+1}$ which is a linear polynomial in the paper is then set to be equal to the average of $\mathbf{B}_{\mathcal{W}_h}^{n+1}\left(x(\hat{\eta}_{\hat{\imath}}), y(\hat{\eta}_{\hat{\imath}})\right) \cdot \boldsymbol{\nu}_{\hat{\imath}}^{\mathcal{T}}$ over edge $e_{\hat{\imath}}^{\mathcal{T}}$ to conserve the flux, and the second moment of $b_{\mathcal{T}}^{(\hat{\imath}),n+1}$ can be obtained by averaging the second moments of the $\mathbf{B}_{\mathcal{W}_h}^{n+1}\left(x(\hat{\eta}_{\hat{\imath}}), y(\hat{\eta}_{\hat{\imath}})\right) \cdot \boldsymbol{\nu}_{\hat{\imath}}^{\mathcal{T}}$ on the two dual cells crossed by $e_{\hat{\imath}}^{\mathcal{T}}$.

Let $(B_{x,i}, B_{y,i})^t$ be $\mathbf{B}_{\mathcal{T}_h}^{n+1}$ restricted on triangular cell $\mathcal{K}_i$, and be represented by

$$\begin{cases} B_{x,i}(x, y) = a_{0,i} + a_{1,i}x + a_{2,i}y \ , \\ B_{y,i}(x, y) = b_{0,i} + b_{1,i}x + b_{2,i}y \ . \end{cases} \tag{3.34}$$

The divergence-free condition $\nabla \cdot (B_{x,i}, B_{y,i})^t = 0$ gives the equation:

$$a_{1,i} = -b_{2,i} \ . \tag{3.35}$$

On each edge $e_{l,i}^{\mathcal{T}}$ of $\mathcal{K}_i$, $(B_{x,i}, B_{y,i})^t$ is required to satisfy:

$$\left((B_{x,i}, B_{y,i})^t \cdot \boldsymbol{\nu}_{l,i}^{\mathcal{T}}\right)(\hat{\eta}_{\hat{\imath}}) = b_{\mathcal{T}}^{(\hat{\imath}),n+1}(\hat{\eta}_{\hat{\imath}}) \ , \qquad l = 1, 2, 3 \ . \tag{3.36}$$

Note that one equation of the condition (3.36), namely, the first moment of $\left((B_{x,i}, B_{y,i})^t \cdot \boldsymbol{\nu}_{1,i}^{\mathcal{T}}\right)(\hat{\eta}_i)$ is equal to the first moment of $b_{\mathcal{T}}^{(i),n+1}(\hat{\eta}_i)$ on $e_{1,i}^{\mathcal{T}}$, is redundant because condition (3.35) already implies that the net influx across the boundary of $\mathcal{K}_i$ is zero. Solving Eqs. (3.35)-(3.36) for $a_{0,i}, \ldots, a_{2,i}$ and $b_{0,i}, \ldots, b_{2,i}$ uniquely determines $(B_{x,i}, B_{y,i})^t$ on $\mathcal{K}_i$ at time level t^{n+1}.

On each cell of $\mathcal{T}_h$, the above procedure is applied to reconstruct a divergence-free magnetic field. $\mathbf{B}_{\mathcal{T}_h}^{n+1}$ is defined as

$$\mathbf{B}_{\mathcal{T}_h}^{n+1}\Big|_{\mathbf{x}\in\mathcal{K}_i} = (B_{x,i}, B_{y,i})^t \ , \qquad i = 1, \ldots, \mathcal{N}_{\mathcal{T}} \ .$$

Moreover, for any two cells $\mathcal{K}_i$ and $\mathcal{K}_{i'}$ sharing a common edge $e_{\hat{i}}^{\mathcal{T}}$, $(B_{x,i}, B_{y,i})^t$ and $(B_{x,i'}, B_{y,i'})^t$ defined on the two cells have the same normal component of the magnetic field on $e_{\hat{i}}^{\mathcal{T}}$. Therefore $\mathbf{B}_{\mathcal{T}_h}^{n+1}$ is exactly divergence-free.

When the solution contains discontinuities, a limiting procedure is needed. The limiting algorithm for reconstructing the central DG solution is outlined in Sec. 5.

4 Central Scheme Formulation for Solving Ideal MHD Equations

The central DG formulation discussed in the previous section can also be done similarly with a finite volume version.

Let $\overline{U}_{h,k}^{(i)}(t)$ be the cell average of the $k^{th}(k = 1, \ldots, 6)$ component of the approximate solution of $\mathbf{U}(\mathbf{x}, t)$ on $\mathcal{K}_i$. The semi-discrete finite volume scheme for solving $\overline{U}_{h,k}^{(i),n+1} \equiv \overline{U}_{h,k}^{(i)}(t = t^{n+1})$ on cell $\mathcal{K}_i$ is

$$\frac{d}{dt}\overline{U}_{h,k}^{(i)}(t) = -\frac{1}{|\mathcal{K}_i|}\sum_{e\in\partial\mathcal{K}_i}\int_e h_{e,k}(\mathbf{x}, t)d\Gamma \ , \qquad \forall\mathcal{K}_i \in \mathcal{T}_h \ , \tag{4.1}$$

where $h_{e,k}(\mathbf{x}, t)$ is defined in Eq. (3.13).

Let $\overline{B}_{\mathcal{T}_h,\blacklozenge}^{(i)}(t)$ be the cell average of the x- or y-component (indicated by $\blacklozenge$) of the approximate solution of $\mathbf{B}^B(\mathbf{x}, t)$ on $\mathcal{K}_i$. The semi-discrete central scheme for solving $\overline{B}_{\mathcal{T}_h,\blacklozenge}^{n+1} \equiv \overline{B}_{\mathcal{T}_h,\blacklozenge}^{(i)}(t = t^{n+1})$ on cell $\mathcal{K}_i$ is

$$\begin{aligned}\tfrac{d}{dt}\overline{B}_{\mathcal{T}_h,\blacklozenge}^{(i)}(t)\Big|_{t=t^n} &= \frac{1}{\triangle\tau^n}\left(\frac{1}{|\mathcal{K}_i|}\int_{\mathcal{K}_i} B_{\mathcal{W}_h,\blacklozenge}(\mathbf{x}, t^n)d\mathbf{x} - \overline{B}_{\mathcal{T}_h,\blacklozenge}^{(i)}(t^n)\right) \\ &- \frac{1}{|\mathcal{K}_i|}\sum_{e\in\partial\mathcal{K}_i}\int_e \left(F_{\blacklozenge}^B(\mathbf{U}_{\mathcal{T}_h}, \mathbf{B}_{\mathcal{W}_h}), G_{\blacklozenge}^B(\mathbf{U}_{\mathcal{T}_h}, \mathbf{B}_{\mathcal{W}_h})\right)\cdot\boldsymbol{\nu}_{e,i}d\Gamma \\ &\qquad\qquad \forall\mathcal{K}_i \in \mathcal{T}_h \ .\end{aligned} \tag{4.2}$$

Note that

$$\overline{B}_{\mathcal{T}_h,\blacklozenge}^{(i)}(t^n) = \frac{1}{|\mathcal{K}_i|}\int_{\mathcal{K}_i} B_{\mathcal{T}_h,\blacklozenge}(\mathbf{x}, t^n)d\mathbf{x}$$

with $(B_{\mathcal{T}_h,x}(\mathbf{x}, t^n), B_{\mathcal{T}_h,y}(\mathbf{x}, t^n))^t \equiv \mathbf{B}_{\mathcal{T}_h}^n$. And $(B_{\mathcal{W}_h,x}(\mathbf{x}, t^n), B_{\mathcal{W}_h,y}(\mathbf{x}, t^n))^t \equiv \mathbf{B}_{\mathcal{W}_h}^n$.

Let $\overline{b}^{(j)}_{\mathcal{W}_h}(\cdot,t)$ be the approximation to the edge average of the normal component of the magnetic field (in $\boldsymbol{\nu}_j$ direction) on edge $e_j^{\mathcal{W}}$ of grid $\mathcal{W}_h$. $\overline{b}^{(j)}_{\mathcal{W}_h}(\cdot,t)$ is obtained by solving the first equation of (3.21).

The semi-discrete central scheme for solving $\overline{b}^{(j)}_{\mathcal{W}_h}(\cdot,t^{n+1})$ is

$$\frac{d}{dt}\overline{b}^{(j)}_{\mathcal{W}_h}(t)\,\Big|_{t=t^n} = \frac{1}{\triangle\tau^n}\left(\overline{b}^{(j)}_{\mathcal{T}_h}(t^n) - \overline{b}^{(j)}_{\mathcal{W}_h}(t^n)\right) - \frac{2}{\mid e_j^{\mathcal{W}} \mid}\left(E_{z,\mathcal{T}_h}(\hat{\zeta}_j)\,\Big|_{-1}^{1}\right)\ , \qquad \forall e_j^{\mathcal{W}} \in \mathcal{L}_h\ , \tag{4.3}$$

where $\overline{b}^{(j)}_{\mathcal{T}_h}(t^n)$ is the edge average of the normal component of $\mathbf{B}^n_{\mathcal{T}_h}$ (in $\boldsymbol{\nu}_j$ direction) on $e_j^{\mathcal{W}}$. A closed form of the central scheme is outlined as follows.

Algorithm 2: Numerical Algorithm of Central Scheme

- **Computation** sub-step: suppose $\mathbf{U}^n_{\mathcal{T}_h}$, $\mathbf{B}^n_{\mathcal{W}_h}$ and $\mathbf{B}^n_{\mathcal{T}_h}$ are given.
  1. Compute cell averages $\{\overline{U}^{(i)}_{h,k}(t^{n+1})\}$ and $\{\overline{B}^{(i)}_{\mathcal{T}_h,\blacklozenge}(t^{n+1})\}$ supported on grid cells of $\mathcal{T}_h$.
  2. Compute edge averages $\{\overline{b}^{(j)}_{\mathcal{W}_h}(t^{n+1})\}$ supported on grid edges of $\mathcal{W}_h$.
- **Reconstruction** sub-step: suppose $\{\overline{U}^{(i)}_{h,k}(t^{n+1})\}$, $\{\overline{B}^{(i)}_{\mathcal{T}_h,\blacklozenge}(t^{n+1})\}$ and $\{\overline{b}^{(j)}_{\mathcal{W}_h}(t^{n+1})\}$ are given.
  1. Reconstruct piecewise linear $\mathbf{U}^{n+1}_{\mathcal{T}_h}$ and $\mathbf{B}^{n+1}_{\mathcal{T}_h,loc} \in \boldsymbol{\mathcal{B}}_{\mathcal{T}_h,loc}$ on grid $\mathcal{T}_h$ by using cell averages $\{\overline{U}^{(i)}_{h,k}(t^{n+1})\}$ and $\{\overline{B}^{(i)}_{\mathcal{T}_h,\blacklozenge}(t^{n+1})\}$ respectively.
  2. Reconstruct piecewise linear $b^{n+1}_{\mathcal{W}_h}$ by using $\{\overline{b}^{(j)}_{\mathcal{W}_h}(t^{n+1})\}$ and $\mathbf{B}^{n+1}_{\mathcal{T}_h,loc}$.
  3. Reconstruct $\mathbf{B}^{n+1}_{\mathcal{W}_h} \in \boldsymbol{\mathcal{B}}_{\mathcal{W}_h}$ on grid cells of $\mathcal{W}_h$ by using $b^{n+1}_{\mathcal{W}_h}$ and $\mathbf{B}^{n+1}_{\mathcal{T}_h,loc}$.
  4. Reconstruct $\mathbf{B}^{n+1}_{\mathcal{T}_h} \in \boldsymbol{\mathcal{B}}_{\mathcal{T}_h}$ on grid cells of $\mathcal{T}_h$ by using $\mathbf{B}^{n+1}_{\mathcal{W}_h}$.

4.1 Finite volume reconstruction

In Alg. 2, we need to reconstruct piecewise linear functions from given cell averages or edge averages. In this subsection, we solve the following two reconstruction problems for this purpose:

Reconstruction problem 1. Given cell average values $\overline{v}_i$ of a function $v(x,y)$ on each cell $\mathcal{K}_i$, reconstruct an essentially non-oscillatory (ENO) polynomial $v_i(x,y)$ of degree at most 1 on each cell $\mathcal{K}_i$ which has its mean value $\overline{v}_i$ and is a second-order accurate approximation to $v(x,y)$ on $\mathcal{K}_i$ (where $v(x,y)$ is smooth). This is a classical MUSCL or second order ENO reconstruction. The following expression of a first degree polynomial $v_i(x,y)$ supported on $\mathcal{K}_i$ is used:

$$v_i(x,y) = a_{0,i} + a_{1,i}\frac{x-x_i}{|\mathcal{K}_i|} + a_{2,i}\frac{y-y_i}{|\mathcal{K}_i|}\ , \tag{4.4}$$

where (x_i,y_i) is the centroid of $\mathcal{K}_i$.

For the ideal MHD problem, at the end of every Runge-Kutta stage, this reconstruction is used to obtain each component of $\mathbf{U}_{\mathcal{T}_h}(\mathbf{x},t)$ and $\mathbf{B}_{\mathcal{T}_h,loc}(\mathbf{x},t)$.

Reconstruction problem 2. For each grid edge $e_j^{\mathcal{W}}$ of $\mathcal{W}_h$, reconstruct a $b_{\mathcal{W}_h}^{(j)} \in P^1(\hat{\zeta}_j)$ supported on $e_j^{\mathcal{W}}$ such that

$$\frac{1}{2}\int_{-1}^{1} b_{\mathcal{W}_h}^{(j)} \left| \frac{\partial e_j^{\mathcal{W}}(\mathbf{x})}{\partial \hat{\zeta}_j} \right| d\hat{\zeta}_j = \overline{b}_{\mathcal{W}_h}^{(j)} \ .$$

After these two reconstruction problems are solved, the algorithm described in Sec. 3.4 is used to reconstruct exactly divergence-free $\mathbf{B}_{\mathcal{W}_h}^{n+1}$ on $\mathcal{W}_h$. Then the algorithm described in Sec. 3.5 is used to reconstruct exactly divergence-free $\mathbf{B}_{\mathcal{T}_h}^{n+1}$ on $\mathcal{T}_h$.

4.1.1 Reconstructing $\mathbf{U}_{\mathcal{T}_h}(\mathbf{x},t^{n+1})$ and $\mathbf{B}_{\mathcal{T}_h,loc}(\mathbf{x},t^{n+1})$ on cells of $\mathcal{T}_h$

Reconstruction problem 1 is solved as follows. Denote $U_{h,k}^{(i)}(\mathbf{x},t) \in P^1(\mathcal{K}_i)$, the reconstructed k^{th} component of $\mathbf{U}_{\mathcal{T}_h}(\mathbf{x},t)$ on $\mathcal{K}_i$ and $\mathbf{B}_{\mathcal{T}_h,loc}^{(i)}(\mathbf{x},t) \in \mathbf{\Pi}^1(\mathcal{K}_i)$ the reconstructed locally divergence-free magnetic field on $\mathcal{K}_i$, $\mathbf{B}_{\mathcal{T}_h,loc}^{(i)}(\mathbf{x},t) \equiv \left(B_{\mathcal{T}_h,loc,x}^{(i)}(\mathbf{x},t), B_{\mathcal{T}_h,loc,y}^{(i)}(\mathbf{x},t)\right)^t$. And $\mathbf{B}_{\mathcal{T}_h,loc}(\mathbf{x},t)\Big|_{\mathbf{x}\in\mathcal{K}_i} = \mathbf{B}_{\mathcal{T}_h,loc}^{(i)}(\mathbf{x},t)$.

Let $v_i(x,y)$ be either $U_{h,k}^{(i)}(\mathbf{x},t)$ or the x- or y-component of $\left(B_{\mathcal{T}_h,loc,x}^{(i)}(\mathbf{x},t), B_{\mathcal{T}_h,loc,y}^{(i)}(\mathbf{x},t)\right)^t$. Its approximate cell average $\overline{v}_i$ is computed by either Eq. (4.1) or Eq. (4.2). The procedure for reconstructing $v_i(x,y)$ is summarized as follows:

Step 1. For every grid cell $\mathcal{K}_i$, we identify a set of admissible reconstruction stencils $\mathfrak{ST} = \{\mathfrak{T}^{(m)} : m = 1,\dots 10\}$. See Fig. 2 for example. Consider to reconstruct $v_0(x,y)$ on cell $\mathcal{K}_0$. The following $\mathfrak{T}^{(m)}$ are constructed. $\mathfrak{T}^{(1)} = \{\mathcal{K}_0,\mathcal{K}_1,\mathcal{K}_{10}\}$; $\mathfrak{T}^{(2)} = \{\mathcal{K}_0,\mathcal{K}_{20},\mathcal{K}_2\}$; $\mathfrak{T}^{(3)} = \{\mathcal{K}_0,\mathcal{K}_2,\mathcal{K}_{21}\}$; $\mathfrak{T}^{(4)} = \{\mathcal{K}_0,\mathcal{K}_3,\mathcal{K}_{30}\}$; $\mathfrak{T}^{(5)} = \{\mathcal{K}_0,\mathcal{K}_3,\mathcal{K}_{31}\}$; $\mathfrak{T}^{(6)} = \{\mathcal{K}_0,\mathcal{K}_1,\mathcal{K}_{11}\}$; $\mathfrak{T}^{(7)} = \{\mathcal{K}_0,\mathcal{K}_{10},\mathcal{K}_{20}\}$; $\mathfrak{T}^{(8)} = \{\mathcal{K}_0,\mathcal{K}_{21},\mathcal{K}_{30}\}$; $\mathfrak{T}^{(9)} = \{\mathcal{K}_0,\mathcal{K}_{11},\mathcal{K}_{31}\}$; and $\mathfrak{T}^{(10)} = \{\mathcal{K}_0,\mathcal{K}_1,\mathcal{K}_2,\mathcal{K}_3\}$. Other choices of stencils are also acceptable. See discussions in [36, 37, 38] for criterion for choosing these stencils. $\mathfrak{ST}$ is used in the paper for easy implementation. Also note that when $\mathcal{K}_0$ is on the boundary of the domain, some of $\mathfrak{T}^{(m)}$ may not exist.

Step 2. For each stencil $\mathfrak{T}^{(m)}$ $m = 1,\dots,9$, we use cell averages defined on cells contained in the stencil to reconstruct preliminarily a $P^1(x,y)$ function $v_i^{(m)}(x,y)$. This is implemented by solving the following system of linear equations for coefficients $a_{0,i}$, $a_{1,i}$ and $a_{2,i}$ of $v_i^{(m)}(x,y)$:

$$\int_{\mathcal{K}_{(m),s}} v_i^{(m)}(x,y)dxdy = |\mathcal{K}_{(m),s}|\overline{v}_{(m),s} \ , s = 1,2,3 \ .$$

Here $\mathcal{K}_{(m),s}$ stands for a cell in $\mathfrak{T}^{(m)}$ and $\overline{v}_{(m),s}$ is its given cell average.

For stencil $\mathfrak{T}^{(10)}$, $v_i^{(10)}(x,y)$ is constructed by constrained least-squares fitting so that

$$\int_{\mathcal{K}_i} v_i^{(10)}(x,y)dxdy = |\mathcal{K}_i|\overline{v}_i \ .$$

Step 3. For each preliminarily reconstructed $v_i^{(m)}(x,y)$, a smoothness indicator ω_m is computed with $\sum_{m=1}^{10}\omega_m = 1$ using the method introduced in [40]. The nonlinearly stabilized reconstruction $v_i(x,y)$ is defined by a weighted combination $\sum_{m=1}^{10}\omega_m v_i^{(m)}$.

The following correction is used to make $(B^{(i)}_{\mathcal{T}_h,loc,x}(\mathbf{x},t), B^{(i)}_{\mathcal{T}_h,loc,y}(\mathbf{x},t))^t$ locally divergence-free, namely $\nabla\cdot(B^{(i)}_{\mathcal{T}_h,loc,x}(\mathbf{x},t), B^{(i)}_{\mathcal{T}_h,loc,y}(\mathbf{x},t))^t = 0$. Let

$$B^{(i)}_{\mathcal{T}_h,loc,x}(\mathbf{x},t) = a^x_{0,i} + a^x_{1,i}\frac{x-x_i}{|\mathcal{K}_i|} + a^x_{2,i}\frac{y-y_i}{|\mathcal{K}_i|}$$

and

$$B^{(i)}_{\mathcal{T}_h,loc,y}(\mathbf{x},t) = a^y_{0,i} + a^y_{1,i}\frac{x-x_i}{|\mathcal{K}_i|} + a^y_{2,i}\frac{y-y_i}{|\mathcal{K}_i|}$$

before the correction.

Denote $a = \min(|a^x_{1,i}|, |a^y_{2,i}|)$. If $a = |a^x_{1,i}|$, then $B^{(i)}_{\mathcal{T}_h,loc,x}(\mathbf{x},t)$ and $B^{(i)}_{\mathcal{T}_h,loc,y}(\mathbf{x},t)$ are modified to be

$$B^{(i)}_{\mathcal{T}_h,loc,x}(\mathbf{x},t) = a^x_{0,i} + a^x_{1,i}\frac{x-x_i}{|\mathcal{K}_i|} + a^x_{2,i}\frac{y-y_i}{|\mathcal{K}_i|}\ ,$$

$$B^{(i)}_{\mathcal{T}_h,loc,y}(\mathbf{x},t) = a^y_{0,i} + a^y_{1,i}\frac{x-x_i}{|\mathcal{K}_i|} - a^x_{1,i}\frac{y-y_i}{|\mathcal{K}_i|}\ ;$$

otherwise, $B^{(i)}_{\mathcal{T}_h,loc,x}(\mathbf{x},t)$ and $B^{(i)}_{\mathcal{T}_h,loc,y}(\mathbf{x},t)$ are modified to be

$$B^{(i)}_{\mathcal{T}_h,loc,x}(\mathbf{x},t) = a^x_{0,i} - a^y_{2,i}\frac{x-x_i}{|\mathcal{K}_i|} + a^x_{2,i}\frac{y-y_i}{|\mathcal{K}_i|}\ ,$$

$$B^{(i)}_{\mathcal{T}_h,loc,y}(\mathbf{x},t) = a^y_{0,i} + a^y_{1,i}\frac{x-x_i}{|\mathcal{K}_i|} + a^y_{2,i}\frac{y-y_i}{|\mathcal{K}_i|}\ .$$

This reconstruction is now complete.

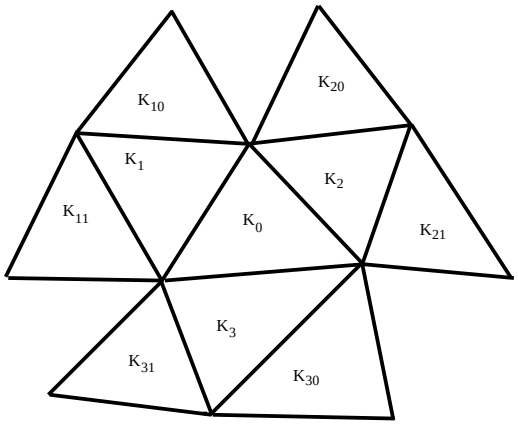

Figure 2: Cells used for reconstructing the second-order accurate polynomial approximations for cell centered variables on cell $\mathcal{K}_0$.

We then proceed to solve the ***Reconstruction problem 2***.

4.1.2 Reconstructing $b^{(\jmath)}_{\mathcal{W}_h}(t^{n+1})$ on grid edges of $\mathcal{W}_h$

Consider an edge $e^{\mathcal{W}}_\jmath$ of grid $\mathcal{W}_h$ which crosses two triangle cells $\mathcal{K}_i$ and $\mathcal{K}_{i'}$ of $\mathcal{T}_h$. See Fig. 1 for example. The grid edge connecting points $V1$ and $V2$ crosses cells $\mathcal{K}1$ and $\mathcal{K}2$. Let the unit edge normal of $e^{\mathcal{W}}_\jmath$ be $\boldsymbol{\nu}^{\mathcal{W}}_\jmath$ and the parametric form of $e^{\mathcal{W}}_\jmath$ be given by Eq. (3.22).

The normal component of $\mathbf{B}_{\mathcal{T}_h,loc}(\mathbf{x}, t^{n+1})$ (in $\boldsymbol{\nu}^{\mathcal{W}}_\jmath$ direction) on part of the edge $e^{\mathcal{W}}_\jmath$ which is on cell $\mathcal{K}_i$ is

$$b_i(\hat{\zeta}_\jmath, t^{n+1}) = \boldsymbol{\nu}^{\mathcal{W}}_\jmath \cdot \mathbf{B}^{(i)}_{\mathcal{T}_h,loc}\left(x(\hat{\zeta}_\jmath), y(\hat{\zeta}_\jmath), t^{n+1}\right) \ . \tag{4.5}$$

$b_i(\hat{\zeta}_\jmath, t^{n+1})$ is a linear polynomial with respect to parameter $\hat{\zeta}_\jmath$. Here $e^{\mathcal{W}}_\jmath$ is parameterized by $\mathbf{x}(\hat{\zeta}_\jmath)$.

Similarly the normal component of $\mathbf{B}_{\mathcal{T}_h,loc}(\mathbf{x}, t^{n+1})$ on part of the edge $e^{\mathcal{W}}_\jmath$ which is on cell $\mathcal{K}_{i'}$ along $\mathbf{x}(\hat{\zeta}_\jmath)$ is

$$b_{i'}(\hat{\zeta}_\jmath, t^{n+1}) \ = \boldsymbol{\nu}^{\mathcal{W}}_\jmath \cdot \mathbf{B}^{(i')}_{\mathcal{T}_h,loc}\left(x(\hat{\zeta}_\jmath), y(\hat{\zeta}_\jmath), t^{n+1}\right) \ . \tag{4.6}$$

For convenience in discussion let's rewrite $b_i(\hat{\zeta}_\jmath)$ and $b_{i'}(\hat{\zeta}_\jmath)$ in the following forms:

$$\begin{array}{rcll} b_i(\hat{\zeta}_\jmath) & = & a_i + b_i\hat{\zeta}_\jmath \ , & \\ b_{i'}(\hat{\zeta}_\jmath) & = & a_{i'} + b_{i'}\hat{\zeta}_\jmath \ , & -1 \le \hat{\zeta}_\jmath \le 1 \ . \end{array} \tag{4.7}$$

Finally, the reconstructed $b^{(\jmath)}_{\mathcal{W}_h}(t^{n+1})$ supported on $e^{\mathcal{W}}_\jmath$ is defined as

$$b^{(\jmath)}_{\mathcal{W}_h}(\hat{\zeta}_\jmath, t^{n+1}) = \overline{b}^{(\jmath)}_{\mathcal{W}_h}(t^{n+1}) + \hat{b}_\jmath\hat{\zeta}_\jmath \ , \qquad -1 \le \hat{\zeta}_\jmath \le 1 \ , \tag{4.8}$$

where $\hat{b}_\jmath$ is obtained by a weighted combination of b_i and $b_{i'}$ as follows:

$$\alpha_1 = \frac{1.0}{\epsilon + (b_i)^2} \ , \quad \alpha_2 = \frac{1.0}{\epsilon + (b_{i'})^2} \ ,$$

$$\omega_1 = \frac{\alpha_1}{\alpha_1 + \alpha_2} \ , \quad \omega_2 = \frac{\alpha_2}{\alpha_1 + \alpha_2} \ ,$$

$$\hat{b}_\jmath = \omega_1 b_i + \omega_2 b_{i'} \ ,$$

and $\epsilon = 10^{-8}$ in this paper.

5 Limiting Technique

For the central DG scheme, since shock waves or contact discontinuities are all local phenomena, we apply a detector introduced in [41] to identify cells, denoted as "trouble cells" on $\mathcal{T}_h$ which may contain oscillatory solutions. The reconstruction algorithm described in Sec. 4.1.1 is first applied to solutions $\mathbf{U}_{\mathcal{T}_h}(\mathbf{x}, t^{n+1})$ and $\mathbf{B}_{\mathcal{T}_h,loc}(\mathbf{x}, t^{n+1})$ supported on these "trouble cells" of $\mathcal{T}_h$. For other cells of $\mathcal{T}_h$, there is no need to do reconstruction. For the central finite volume scheme, the reconstruction is applied to all cells of $\mathcal{T}_h$ to get $\mathbf{U}_{\mathcal{T}_h}(\mathbf{x}, t^{n+1})$ and $\mathbf{B}_{\mathcal{T}_h,loc}(\mathbf{x}, t^{n+1})$. Then the reconstruction algorithm described in Sec. 4.1.2 is used to

reconstruct $b^{(j)}_{\mathcal{W}_h}(t^{n+1})$ on edges which are on "trouble cells" or intersect "trouble cells". For other edges of $\mathcal{W}_h$, there is no need to do reconstruction for the central DG scheme; and we can take uniform weights $\alpha_1, \alpha_2 = 1$ in the reconstruction described in Sec. 4.1.2 for the central finite volume scheme. Finally, the algorithm described in Sec. 3.4 is used to reconstruct the exactly divergence-free $\mathbf{B}^{n+1}_{\mathcal{W}_h}$ on dual cells. And the algorithm described in Sec. 3.5 is used to reconstruct the exactly divergence-free $\mathbf{B}^{n+1}_{\mathcal{T}_h}$ on $\mathcal{T}_h$ subsequently.

6 Numerical Test Problems

In this section, numerical examples with smooth or discontinuous solutions are presented to demonstrate the performance of the schemes introduced in this paper. The time step size $\triangle t^n$ is dynamically determined by

$$\triangle t^n = \frac{hC_{\mathrm{CFL}}}{\max(|\mathbf{u}| + c)} ,$$

where h is triangle edge length, C_{CFL} is the CFL number and c is the speed of the fast magneto-acoustic wave [6]. With second-order TVD Runge-Kutta time discretization, $C_{\mathrm{CFL}} = 0.1$ is used for all simulations. $\theta = \triangle t^n / \Delta\tau^n = 0.5$ is used in the fully discrete central DG or FV schemes for computing the magnetic field.

6.1 Vortex evolution problem

We consider a vortex evolution problem to test the order of accuracy of the schemes. The vortex problem was initially suggest in [35] and was adapted to the MHD equations in [24]. The problem is defined on a $[-5, 5] \times [-5, 5]$ domain with flow through boundary conditions used on both sides. The unperturbed MHD flow is given by $(\rho, p_{gas}, u_x, u_y, B_x, B_y) = (1, 1, 1, 1, 0, 0)$. The ratio of specific heats is $\gamma = 5/3$. The vortex is introduced through perturbed velocity and magnetic fields given by

$$(\delta u_x, \delta u_y) = \frac{\kappa}{2\pi} e^{0.5(1-r^2)}(-y, x) ,$$

$$(\delta B_x, \delta B_y) = \frac{\mu}{2\pi} e^{0.5(1-r^2)}(-y, x) ,$$

where $r^2 = x^2 + y^2$. The pressure determined by the dynamical balance is given by

$$\delta p_{gas} = \frac{\kappa^2(1 - r^2) - \mu^2}{8\pi^2} e^{1-r^2}.$$

We use $\kappa = 1$, $\mu = 1$ in our computation. The exact solution is the initial configuration propagating with speed $(1, 1)$, and is given by

$$\mathbf{U}(x, y, t) = \mathbf{U}_0(x - t, y - t) ,$$

where $\mathbf{U}_0 = (\rho, p_{gas} + \delta p_{gas}, u_x + \delta u_x, u_y + \delta u_y, B_x + \delta B_x, B_y + \delta B_y)$. The Dirichlet boundary condition with solution on the boundary given by $\mathbf{U}(x, y, t)$ is used. The typical triangle

edge length, denoted by h, is listed in the first column of all the tables shown in this section. Table 1 shows the L_1 and L_∞ errors and orders of accuracy using values of variables ρ and ε at time $T = 1.0$ computed by the second-order central DG scheme. Table 2 shows the L_1 and L_∞ errors and orders of accuracy of B_x on grids $\mathcal{T}_h$ and $\mathcal{W}_h$ respectively. L_1 and L_∞ errors and orders of accuracy using values of variables ρ and ε at time $T = 1.0$ computed by the second-order central FV scheme is displayed in Table 3, and the L_1 and L_∞ errors and orders of accuracy of B_x computed by the central FV scheme on grids $\mathcal{T}_h$ and $\mathcal{W}_h$ respectively is shown in Table 4. These tables show clearly that both DG and FV schemes achieved the expected accuracy property. The absolute value of the undivided divergence of the magnetic field is about $\mathcal{O}(10^{-13})$ in these calculations. The undivided divergence is defined by sum of the divergence inside the element and the normal jump cross cell edges.

Table 1: Numerical errors and convergence order based on ρ and ε for the second-order accurate central DG scheme for solving the 2D vortex evolution problem.

h	L_1 ρ error	order	L_∞ ρ error	order	L_1 ε error	order	L_∞ ε error	order
$\frac{1}{8}$	9.99E-4	-	4.43E-4	-	4.48E-3	-	1.96E-3	-
$\frac{1}{16}$	2.47E-4	2.02	1.09E-4	2.02	1.18E-3	1.92	5.06E-4	1.95
$\frac{1}{32}$	6.30E-5	1.97	2.89E-5	1.92	3.05E-4	1.95	1.70E-4	1.57
$\frac{1}{64}$	1.63E-5	1.95	7.94E-6	1.86	8.30E-5	1.88	4.39E-5	1.95
$\frac{1}{128}$	4.24E-6	1.94	2.39E-6	1.73	2.14E-5	1.96	1.09E-5	2.01

Table 2: Numerical errors and convergence order based on B_x for the second-order accurate central DG scheme for solving the 2D vortex evolution problem.

h	L_1 B_x error on $\mathcal{T}_h$	order	L_∞ B_x error on $\mathcal{T}_h$	order	L_1 B_x error on $\mathcal{W}_h$	order	L_∞ B_x error on $\mathcal{W}_h$	order
$\frac{1}{8}$	5.58E-3	-	1.78E-3	-	4.89E-3	-	1.42E-3	-
$\frac{1}{16}$	1.31E-3	2.09	4.56E-4	1.96	1.15E-3	2.09	3.69E-4	1.94
$\frac{1}{32}$	3.28E-4	2.00	1.41E-4	1.69	2.97E-4	1.95	1.22E-4	1.60
$\frac{1}{64}$	8.27E-5	1.99	3.59E-5	1.97	7.48E-5	1.99	3.11E-5	1.97
$\frac{1}{128}$	2.08E-5	1.99	1.17E-5	1.62	1.92E-5	1.96	9.38-6	1.73

6.2 The field loop advection

We consider the megnetic field loop advection problem proposed in [22]. The following initial condition same as in [10, 14] is used. $(\rho, p_{gas}, u_x, u_y, u_z, B_z) = (1, 1, 2, 1, 1, 0)$. $(B_x, B_y) =$

Table 3: Numerical errors and convergence order based on ρ and ε for the second-order accurate central FV scheme for solving the 2D vortex evolution problem.

h	L_1 ρ error	order	L_∞ ρ error	order	L_1 ε error	order	L_∞ ε error	order
$\frac{1}{8}$	6.85E-3	-	3.18E-3	-	2.07E-2	-	8.36E-3	-
$\frac{1}{16}$	9.83E-4	2.80	7.27E-4	2.13	3.30E-3	2.65	1.87E-3	2.16
$\frac{1}{32}$	1.16E-4	3.08	8.90E-5	3.03	5.52E-4	2.58	2.91E-4	2.68
$\frac{1}{64}$	1.74E-5	2.74	7.31E-6	3.61	1.29E-4	2.10	8.86E-5	1.72
$\frac{1}{128}$	3.83E-6	2.18	1.32E-6	2.47	3.38E-5	1.93	3.62E-5	1.29

Table 4: Numerical errors and convergence order based on B_x for the second-order accurate central FV scheme for solving the 2D vortex evolution problem.

h	L_1 B_x error on $\mathcal{T}_h$	order	L_∞ B_x error on $\mathcal{T}_h$	order	L_1 B_x error on $\mathcal{W}_h$	order	L_∞ B_x error on $\mathcal{W}_h$	order
$\frac{1}{8}$	3.72E-2	-	1.16E-2	-	3.42E-2	-	1.15E-2	-
$\frac{1}{16}$	6.13E-3	2.60	2.97E-3	1.97	5.50E-3	2.64	2.95E-3	1.96
$\frac{1}{32}$	9.03E-4	2.76	4.85E-4	2.61	8.51E-4	2.69	4.77E-4	2.63
$\frac{1}{64}$	1.54E-4	2.55	1.13E-4	2.10	1.47E-4	2.53	1.12E-4	2.09
$\frac{1}{128}$	3.37E-5	2.19	3.93E-5	1.52	3.18E-5	2.21	3.92-5	1.51

$(\frac{\partial A_z}{\partial y}, \frac{-\partial A_z}{\partial x})$, where A_z is the z-component of the magnetic potential

$$A_z = \begin{cases} A_0(R-r) & \text{if } r \le R \\ 0 & \text{if } r > R \end{cases}$$

with $A_0 = 10^{-3}$, $R = 0.3$ and $r = \sqrt{x^2+y^2}$. $\gamma = 5/3$.

The computational domain is $[-1,1] \times [-0.5, 0.5]$. Quasi-uniform triangular mesh is used for this calculation for the ease of applying periodic boundary condition on all sides. The typical edge length of triangles is roughly equal to $\frac{1}{180}$. Solution of the problem is computed to time $T = 10$. Figures 3 and 4 show the z-component of the magnetic potential A_z computed by the central DG and FV schemes over time, respectively. Due to exact divergence-free nature of the numerical magnetic field, symmetry of the numerical A_z is well preserved during the whole time of computation. Numerical dissipation is observed around the center and the boundary of the loop and no oscillation is observed in simulation results. For calculation using the central DG scheme, no limiter is applied. [10] used "whether the z-component of the magnetic field B_z stays around machine zero" as a criterion to demonstrate the importance of the magnetic field being divergence-free in the simulation. Both of our schemes produced the approximated B_z with the magnitude of 10^{-5} while using the exactly divergence-free magnetic field. This is caused by the $\mathcal{O}(10^{-6})$ deviation of the numerical u_z from its exact value 1.

6.3 Rotor problem

This test problem is the second rotor problem described in [28]. The computational domain is $[0,1] \times [0,1]$. $\gamma = 5/3$. A dense rotating disk of fluid is initially placed at the central area of the computational domain, while the ambient fluid is at rest. The initial condition is given by

$$(\rho, p_{gas}, u_x, u_y, u_z, B_x, B_y, B_z) = (\rho(\mathbf{x},0), 0.5, u_x(\mathbf{x},0), u_y(\mathbf{x},0), 0, \frac{2.5}{\sqrt{4\pi}}, 0, 0, 0).$$

Here

$$(\rho(\mathbf{x},0), u_x(\mathbf{x},0), u_y(\mathbf{x},0)) = \begin{cases} 10, & -(y-0.5)/r_0, & (x-0.5)/r_0 & \text{if } r < r_0 \\ 1+9f, & -(y-0.5)f/r, & (x-0.5)f/r & \text{if } r_0 < r < r_1 \\ 1, & 0, & 0, & \text{if } r > r_1 \end{cases}$$

where $r_0 = 0.1$, $r_1 = 0.115$, $f = (r_1 - r)/(r_1 - r_0)$, and $r = \sqrt{(x-0.5)^2 + (y-0.5)^2}$.

The solution at time $t = 0.295$ is computed. Figures 5 and 6 plot the numerical results of the density ρ, pressure p_{gas}, magnetic pressure $(B_x^2 + B_y^2)/2$ and Mach number computed by central DG and FV schemes, respectively. We see that there is virtually no diffusion of the loops boundaries and no oscillations in the magnetic pressure within the loops interior. The zoom-in view of the Mach number of the central FV solution is smoother than that of the central DG solution. See Figures 5(e) and 6(e). This is due to the fact that limiting is only applied to DG solution supported on "trouble cells". The pressure is positive throughout the computational domain. The degradation in the density variable that was previously reported in [19] is not seen in our simulation.

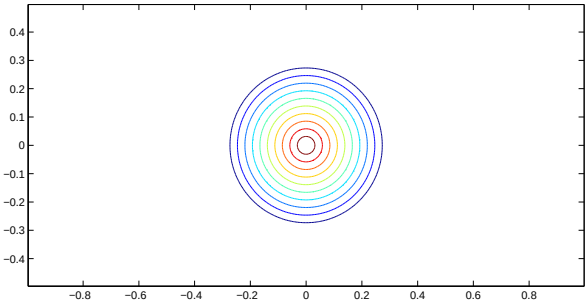

(a)

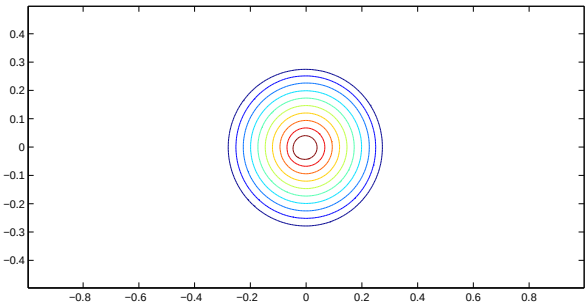

(b)

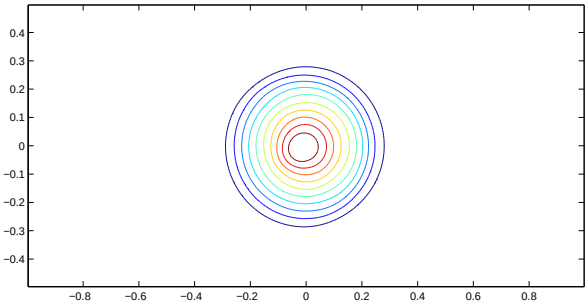

(c)

Figure 3: Central DG solution of the z-component of the magnetic potential A_z of the field loop problem. (a): $t = 0.0$; (b): $t = 2.0$; and (c): $t = 10.0$. 10 equally spaced contours are used.

6.4 Orszag-Tang problem

Here we simulate the Orszag-Tang vortex problem [47]. The initial conditions are $u_x = -\sin(y)$, $u_y = \sin(x)$, $B_x = -\sin(y)$, $B_y = \sin(2x)$, $\rho = \gamma^2$, $p_{gas} = \gamma$, $u_z = B_z = 0$. The computational domain is a square $[0, 2\pi] \times [0, 2\pi]$ with periodic boundary conditions along both boundaries. $\gamma = 5/3$. The final output time $t = \pi$. The typical edge length of triangles used to partition the domain is about $\frac{1}{256}$. Starting from a smooth initial condition, the flow becomes very complex as expected from a transition towards turbulence gradually. Figures 7 and 8 show the development of density ρ solution of the Orszag-Tang vortex

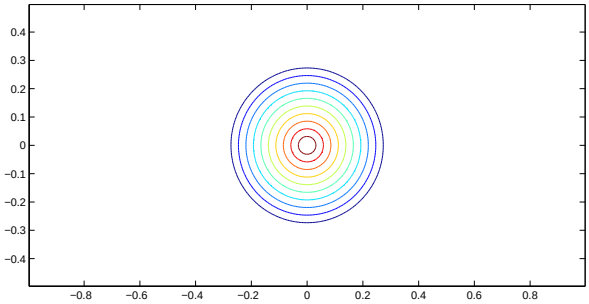

(a)

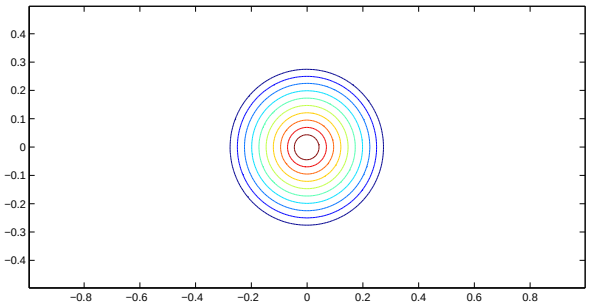

(b)

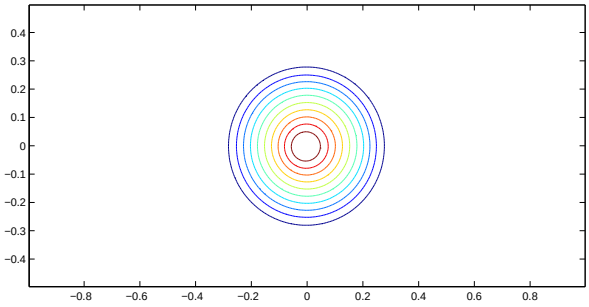

(c)

Figure 4: Central FV solution of the z-component of the magnetic potential A_z of the field loop problem. (a): $t = 0.0$; (b): $t = 2.0$; and (c): $t = 10.0$. 10 equally spaced contours are used.

problem computed by the central DG and FV schemes, respectively. The central DG and FV solutions are comparable. Also we report that the density and pressure have remained positive till at least time $t = 3\pi$. No positivity fix was needed for this problem.

7 Concluding Remarks

In this paper we introduced new central and central DG schemes for solving the ideal MHD equations on two-dimensional triangular grids. These schemes utilized ideas of the CT

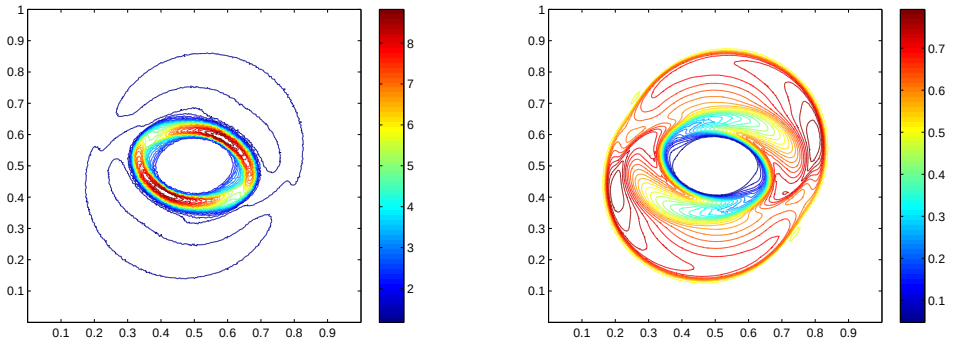

(a)

(b)

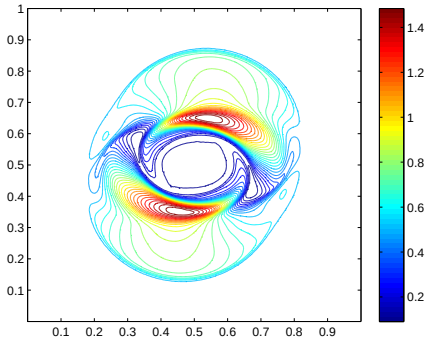

(c)

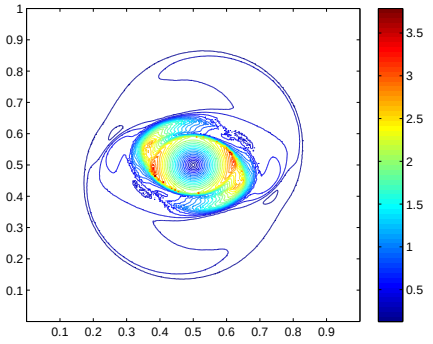

(d)

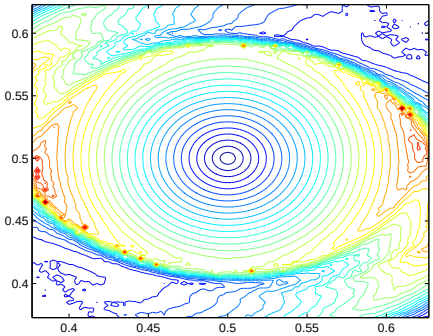

(e)

Figure 5: central DG solution of the rotor problem at time $t = 0.295$. Thirty equally spaced contours are shown in each plot. (a) Density ρ; (b) Pressure p_{gas}; (c) Magnetic pressure $(B_x^2 + B_y^2)/2$; (d) Mach number; (e) Zoom-in view of Mach number around central region.

framework and central schemes and central DG schemes on overlapping cells, and achieve exactly divergence-free magnetic field. Numerical tests show that the proposed schemes have achieved the desired order of accuracy and computed MHD shock wave problems successfully.

While this paper only implements the second-order accurate schemes, the proposed schemes in principle can be generalized to three dimensions and to general meshes with

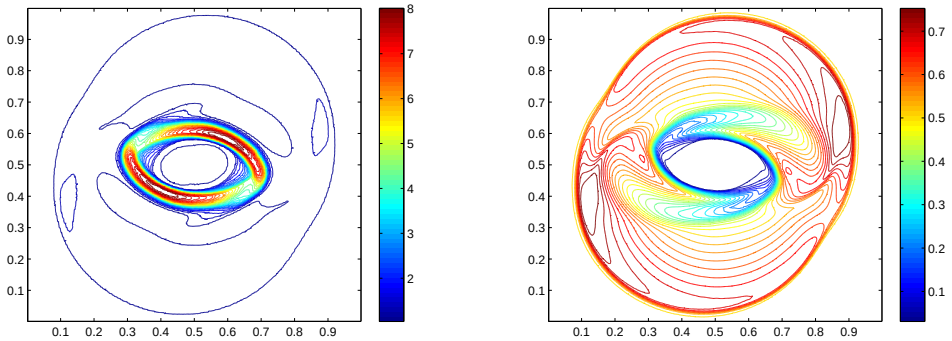

(a)

(b)

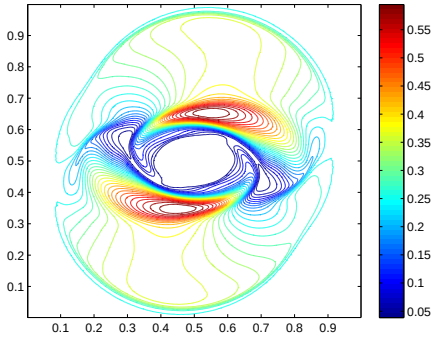

(c)

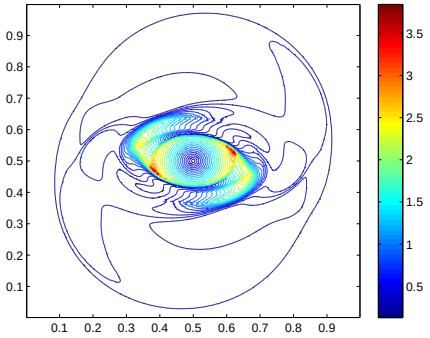

(d)

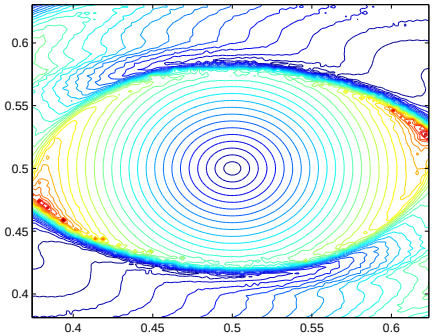

(e)

Figure 6: central FV solution of the rotor problem at time $t = 0.295$. Thirty equally spaced contours are shown in each plot. (a) Density ρ; (b) Pressure p_{gas}; (c) Magnetic pressure $(B_x^2 + B_y^2)/2$; (d) Mach number; (e) Zoom-in view of Mach number around central region.

arbitrary order of accuracy. We will report in a subsequent paper implementation of these schemes with higher-order accuracy.

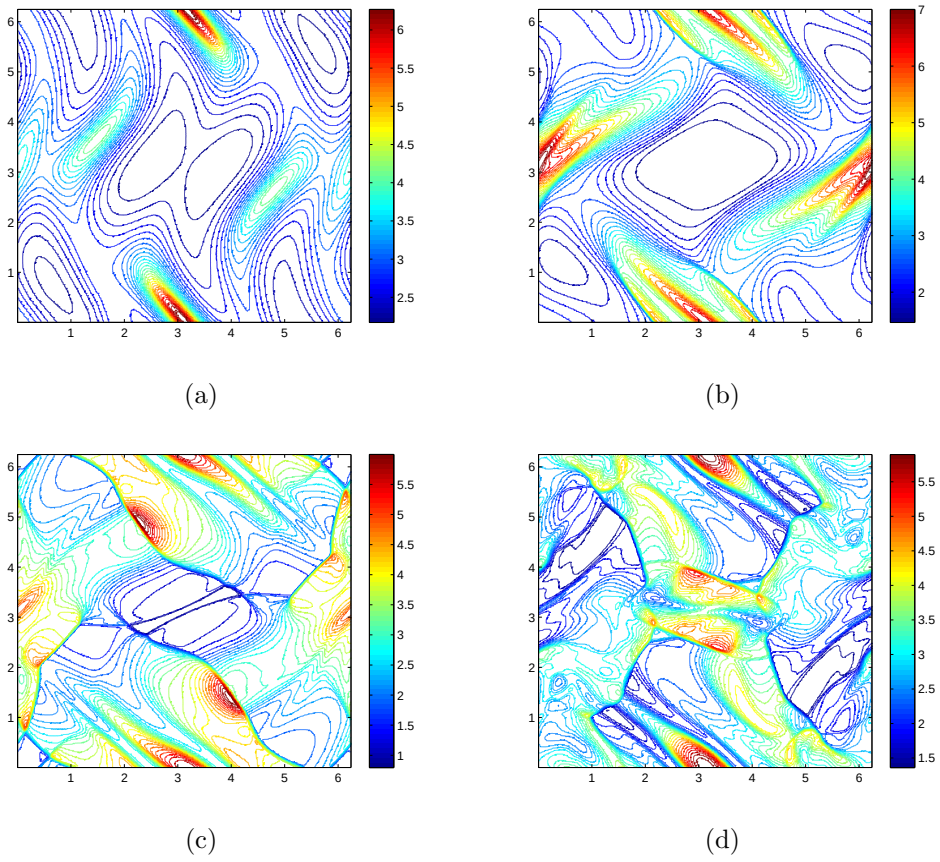

(a) (b)

(c) (d)

Figure 7: Central DG solution of the Orszag-Tang problem. Evolution of ρ over time is plotted by using 15 equally spaced contours. Top left: $t = 0.5$; top right: $t = 1.0$; bottom left: $t = 2.0$; bottom right: $t = 3.14$.

References

[1] T. Miyoshi and K. Kusano. A multi-state HLL approximate Riemann solver for ideal magnetohydrodynamics. *J. Comput. Phys.*, 208:315–344, 2005.

[2] D.S. Balsara. Multidimentional HLLE Riemann solver: Application to Euler and magnetohydrodynamic flows. *J. Comput. Phys.*, 229:1970–1993, 2010.

[3] J.U. Brackbill and D.C. Barnes. The effect of nonzero $\nabla \cdot B$ on the numerical solution of the magnetohydrodynamic equations. *J. Comput. Phys.*, 35:426–430, 1980.

[4] Patricia Cargo and Gérard Gallice. Roe Matrices for Ideal MHD and Systematic Construction of Roe Matrices for Systems of Conservation Laws. *J. Comput. Phys.*, 136:446–466, 1997.

[5] B. Cockburn, S. Hou and C.-W. Shu. The TVB Runge-Kutta local projection discontinuous Galerkin finite element method for conservation laws IV: the multidimensional case. *Math. Comp.*, 54:545–581, 1990.

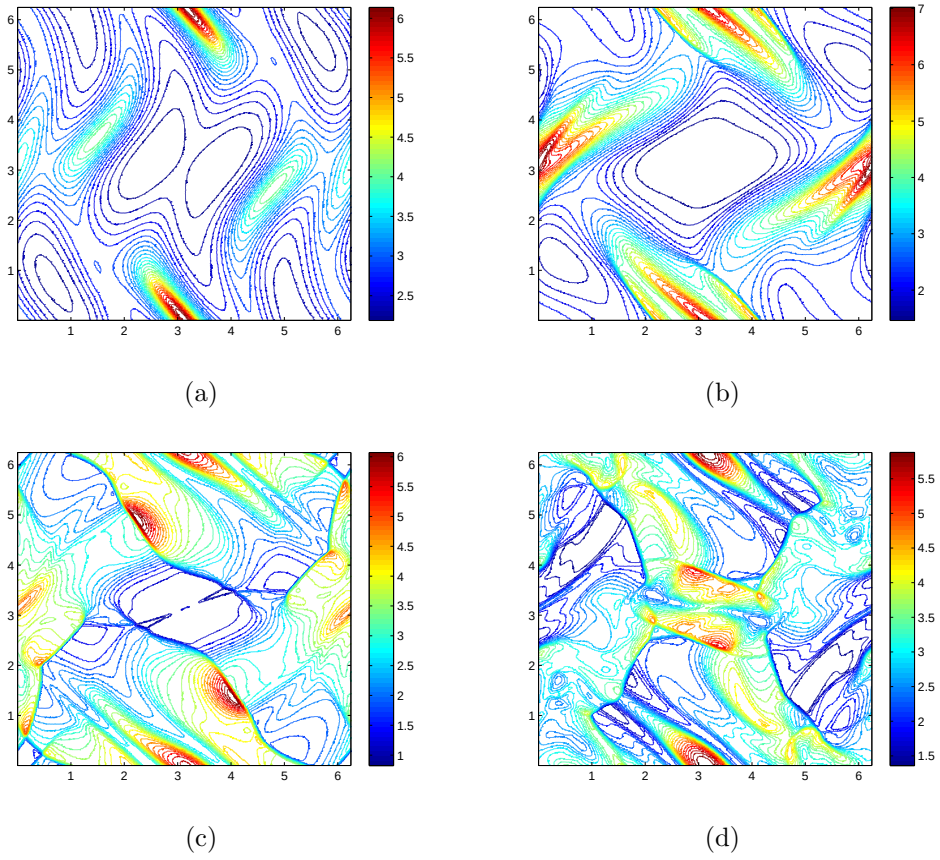

(a) (b)

(c) (d)

Figure 8: Central FV solution of the Orszag-Tang problem. Evolution of ρ over time is plotted by using 15 equally spaced contours. Top left: $t = 0.5$; top right: $t = 1.0$; bottom left: $t = 2.0$; bottom right: $t = 3.14$.

[6] K.G.Powell. An Approximate Riemann Solver for Magnetohydrodynamics (That Works in More Than One Dimension). *Technical Report ICASE Report 194902*, 94-24, ICASE, NASA Langley, 1994.

[7] J. Brackbill. Fluiding modeling of magnetized plasmas. *Space Sci. Rev.*, 42:153, 1985.

[8] S. Gottlieb and C.-W. Shu Total Variation Diminshing Runge-Kutta Schemes. *Mathematics of Computation*, 67(221):73-85, 1998.

[9] G.-S. Jiang, D. Levy, C.-T. Lin, S. Osher and E. Tadmor. High-Resolution Nonoscillatory Central Schemes with Nonstaggered Grids for Hyperbolic Conservatoon Laws. *SIAM J.Numer. Anal.*, 35(6):2147-2168, 1998.

[10] S. Li. High order central scheme on overlapping cells for magneto-hydrodynamic flows with and without constrained transport method. *J. Comput. Phys.*, 227:7368–7393, 2008.

[11] S. Li. A fourth-order divergence-free method for MHD flows. *J. Comput. Phys.*, 229(20):7893–7910, 2010.

[12] F. Li and C.-W. Shu. Locally divergence-free discontinuous Galerkin methods for MHD equations. *Journal of Scientific Computing*, 22-23:413–442, 2005.

[13] B. Cockburn, F. Li and C.-W. Shu. Locally divergence-free discontinuous Galerkin methods for the Maxwell equations. *J. Comput. Phys.*, 22-23:413–442, 2005.

[14] F. Li, L. Xu and S. Yakovlev. Central discontinuous Galerkin methods for ideal MHD equations with the exactly divergence-free magnetic field. *J. Comput. Phys.*, 230:4828–4847, 2011.

[15] F. Li and L. Xu. Arbitrary order exactly divergence-free central discontinuous Galerkin methods for ideal MHD equations. *J. Comput. Phys.*, 231:2655–2675, 2012.

[16] Y. Liu. Central Schemes on Overlapping Cells. *J. Comput. Phys.*, 209:82–104, 2005.

[17] Y. Liu, C.-W. Shu, E. Tadmor and M. Zhang. Central Discontinuous Galerkin Methods on Overlapping Cells with a Non-Oscillatory Hierarchical Reconstruction. *SIAM J. Numer. Anal.*, 45:2442–2467, 2007.

[18] X.-D. Liu and Stanley Osher. Nonoscillatory high order accurate self-similar maximum principle satisfying shock capturing schemes. *SIAM J. Numer. Anal.*, 33(2):760–779, 1996.

[19] P. Londrillo and L. DelZanna. On the divergence-free condition in Godunov-type schemes for ideal magnetohydrodynamics: the upwind constrained transport method. *J. Comput. Phys.*, 195:17–48, 2004.

[20] K.S. Yee. Numerical solution of initial boundary value problems involving Maxwell's equatons in isotropic media. *IEEE Transactions on Antenna Propagation*, AP-14:302–307,1966.

[21] S.H. Brecht, J.G. Lyo, J.A. Fedder and K. Hain. A simulation study of east-west IMF effets on the magnetosphere. *Geophysical Research Letters.*, 8:397–400, 1981.

[22] T.A. Gardiner and J.M. Stone. An unsplit Godunov method for ideal MHD via constrained transport. *J. Comput. Phys.*, 205:509–539, 2005.

[23] J.M. Stone and M.L. Norman. ZEUS-2D: A radiation magnetohydrodynamics code for astrophysical flows in two space dimensions. II The magnetohydrodynamic algorithms and tests. *Astrophysical Journal Supplement Series.*, 80:791-818, 1992.

[24] D.S. Balsara. Second-Order-Accurate Schemes for Magnetohydrodynamics with Divergence-Free Reconstruction. *The Astrophysical Journal Supplement Series*, 151:149–184, 2004.

[25] A. Dedner, F. Kemm, D. Kroner, C.D. Munz, T. Schnitzer and M. Wesenberg. Hyperbolic divergence-cleaning for the MHD equations. *J. Comput. Phys.*, 175:645, 2002.

[26] S. Gottlieb, C.-W. Shu and E. Tadmor. Strong stability-preserving high-order time discretization methods. *SIAM Rev.*, 43(1):89–112, 2001.

[27] H. Nessyahu and E. Tadmor. Non-oscillatory central differencing for hyperbolic conservation laws. *J. Comput. Phys.*, 87:408–463, 1990.

[28] Gabor Toth. The $\nabla \cdot B = 0$ constraint in shock-capturing magnetohydrodynamics codes. *J. Comput. Phys.*, 161:605–652, 2000.

[29] C.-W. Shu and S. Osher. Efficient implementation of essentially non-scillatory capturing schemes. *J. Comput. Phys.*, 77:439–471, 1988.

[30] D.S. Balsara, Chad Meyer, Michael Dumbser, Huijing Du and Zhiliang Xu. Efficient Implementation of ADER Schemes for Euler and Magnetohydrodynamical Flows on Structured Meshes C Comparison with Runge-Kutta Methods. *J. Comput. Phys.*, submitted, 2010.

[31] D.S. Balsara and D. Spicer. Maintaining pressure positivity in magnetohydrodynamic simulations. *J. Comput. Phys.*, 148:133-148, 1999.

[32] D.S. Balsara, T. Rumpf, M. Dumbser and C.D. Munz. Efficient, High Accuracy ADER-WENO Schemes for Hydrodynamics and Divergence-Free MHD. *J. Comput. Phys.*, 228:2480–2516, 2009.

[33] D.S. Balsara Divergence-free reconstruction of magnetic fields and WENO schemes for magnetohydrodynamics. *J. Comput. Phys.*, 228(14):5040–5056, 2009.

[34] D.S. Balsara and D. Spicer. A Staggered mesh Algorithm Using High Order Godunov Fluxes to Ensure Solenoidal Magnetic Fields in Magnetohydrodynamic Simulations. *J. Comput. Phys.*, 149:270–292, 1999.

[35] C.-W. Shu. Essentially non-oscillatory and weighted essentially non-oscillatory schemes for hyperbolic conservation laws. *In Advanced Numerical Approximation of Nonlinear Hyperbolic Equations, B. Cockburn, C. Johnson, C.-W. Shu and E. Tadmor (Editor: A. Quarteroni), Lecture Notes in Mathematics, Berlin. Springer*, 1697, 1998.

[36] A. Harten and S. Chakravarthy. Multi-dimensional ENO schemes for general geometries. *Technical Report* 91–76, ICASE, 1991.

[37] M. Käser and A. Iske. ADER schemes on adaptive triangular meshes for scalar conservation laws. *J. Comput. Phys.*, 205(2):486–508, 2005.

[38] M. Dumbser and M. Käser. Arbitrary high order non-oscillatory finite volume schemes on unstructured meshes for linear hyperbolic systems. *J. Comput. Phys.*, 221:693–723, 2007.

[39] C. Evans and J. Hawley. Simulation of magnetohydrodynamic flows - A constrained transport method. *Astrophysical Journal*, 332:659–677, 1988.

[40] O. Friedrich. Weighted essentially non-oscillatory schemes for the interpolation of mean values on unstructured grids. *J. Comput. Phys.*, 144:194–212, 1998.

[41] B. Cockburn and C.-W. Shu. The TVB Runge-Kutta local projection discontinuous Galerkin finite element method for conservation laws V: multidimensional systems. *J. Comput. Phys.*, 141:199–224, 1998.

[42] D.S. Balsara. Multidimensional HLLE Riemann solver: Application to Euler and magnetohydrodynamic flows. *J. Comput. Phys.*, 229:1970–1993, 2010.

[43] D.S. Balsara, M. Dumbser and R. Abgrall. Multidimensional HLLC Riemann solver for unstructured meshes - With application to Euler and MHD flows. *J. Comput. Phys.*, 261:172–208, 2014.

[44] D.S. Balsara. A two-dimensional HLLC Riemann solver for conservation laws: Application to Euler and magnetohydrodynamic flows. *J. Comput. Phys.*, 231(22):7476–7503, 2012.

[45] D.S. Balsara and M. Dumbser. Divergence-Free MHD on Unstructured Meshes using High Order Finite Volume Schemes Based on Multidimensional Riemann Solvers. *J. Comput. Phys.*, 299:687–715, 2015.

[46] D.S. Balsara and M. Dumbser. Multidimensional Riemann Problem with Self-Similar Internal Structure Part II Application to Hyperbolic Conservation Laws on Unstructured Meshes. *J. Comput. Phys.*, 287:269–292, 2015.

[47] S.A. Orszag and C.M. Tang. Small-scale structure of two-dimensional magnetohydrodynamic turbulence. *J. Fluid Mech.*, 90:129, 1979.

[48] Z.L. Xu, D.S. Balsara and H. Du. Divergence-free WENO reconstruction-based finite volume scheme for solving ideal MHD equations on triangular meshes. *Commun. Comput. Phys.*, 19(4):841–880, 2016.